Monthly Notices of the ROYAL ASTRONOMICAL SOCIETY

MNRAS **467,** 2943–2965 (2017) doi:10.1093/mnras/stx014

Stellar contents and star formation in the NGC 7538 region

Saurabh Sharma,[1]★ A. K. Pandey,[1]★ D. K. Ojha,[2]★ Himali Bhatt,[3] K. Ogura,[4] N. Kobayashi,[5] R. Yadav[6] and J. C. Pandey[1]

[1] *Aryabhatta Research Institute of Observational Sciences (ARIES), Manora Peak, Nainital 263 002, India*
[2] *Tata Institute of Fundamental Research, Homi Bhabha Road, Colaba, Mumbai 400 005, India*
[3] *Inspire faculty, Astrophysical Sciences Division, Bhabha Atomic Research Centre, Trombay, Mumbai 400085, India*
[4] *Kokugakuin University, Higashi, Shibuya-ku, Tokyo 150-8440, Japan*
[5] *Institute of Astronomy, University of Tokyo, 2-21-1 Osawa, Mitaka, Tokyo 181-0015, Japan*
[6] *National Astronomical Research Institute of Thailand, Chiang Mai, Thailand*

Accepted 2017 January 4. Received 2016 December 21; in original form 2016 May 18

ABSTRACT

Deep optical photometric data on the NGC 7538 region were collected and combined with archival data sets from the *Chandra*, 2MASS and *Spitzer* surveys to generate a new catalogue of young stellar objects (YSOs) including those not showing infrared excess emission. This new catalogue is complete down to 0.8 $M_{\odot}$. The nature of the YSOs associated with the NGC 7538 region and their spatial distribution are used to study the star-formation process and the resultant mass function (MF) in the region. Out of the 419 YSOs, ~91 per cent have ages between 0.1 and 2.5 Myr and ~86 per cent have masses between 0.5 and 3.5 $M_{\odot}$, as derived by the spectral energy distribution fitting analysis. Around 24, 62 and 2 per cent of these YSOs are classified to be class I, class II and class III sources, respectively. The X-ray activities for the class I, class II and class III objects are not significantly different from each other. This result implies that the enhanced X-ray surface flux due to the increase in the rotation rate may be compensated for by the decrease in the stellar surface area during the pre-main-sequence evolution. Our analysis shows that the O3V type high-mass star IRS 6 may have triggered the formation of young low-mass stars up to a radial distance of 3 pc. The MF shows a turn-off at around 1.5 $M_{\odot}$ and the value of its slope Γ in the mass range $1.5 < M/M_{\odot} < 6$ is -1.76 ± 0.24, which is steeper than the Salpeter value.

Key words: stars: formation – stars: pre-main-sequence – H II regions.

1 INTRODUCTION

Observational studies of bubbles associated with H II regions suggest that their expansion probably triggers 14 to 30 per cent of the star formation in our Galaxy (e.g. Deharveng et al. 2010; Thompson et al. 2012; Kendrew et al. 2012). These observational results have revealed the importance of OB stars on star-formation activity on the Galactic scale. Massive stars have a profound effect on their natal environment, creating wind-blown shells, cavities and H II regions. The immense amount of energy released through their stellar winds and radiation disperses and destroys the remaining molecular gas and likely inhibits further star formation. However, it has also been argued that, in some circumstances, the energy feedback by these massive stars can promote and induce subsequent star formation in the surrounding molecular gas before it disperses (Koenig et al. 2012).

Identification and characterization of the young stellar objects (YSOs) in star-forming regions (SFRs) hosting massive stars are essential for examining the physical processes that govern the star formation of the next generation in such regions. One of the notable feedback effects of massive stars is the triggering of star formation of new generations, either by sweeping the neighbouring molecular gas into a dense shell, which subsequently fragments into prestellar cores (e.g. Elmegreen & Lada 1977; Whitworth et al. 1994; Elmegreen 1998), or by compressing pre-existing dense clumps (e.g. Sandford, Whitaker & Klein 1982; Bertoldi 1989; Lefloch & Lazareff 1994). The former process is called collect and collapse and the latter radiation-driven implosion (RDI). The aligned elongated distribution of YSOs with respect to the high-mass stars around the interface of an H II region and a molecular cloud is considered as an observational signature of the RDI process (Ogura, Sugitani & Pickles 2002; Lee et al. 2005), whereas the neutral compressed layer observed as a ring of molecular line emission surrounding the H II region is an observational signature of the collect and collapse process (for details, see Deharveng, Zavagno & Caplan 2005). Dale, Haworth & Bressert (2015) with the help of

---

★ E-mail: saurabh@aries.res.in (SS); pandey@aries.res.in (AKP); ojha@tifr.res.in (DKO)

Published by Oxford University Press on behalf of the Royal Astronomical Society

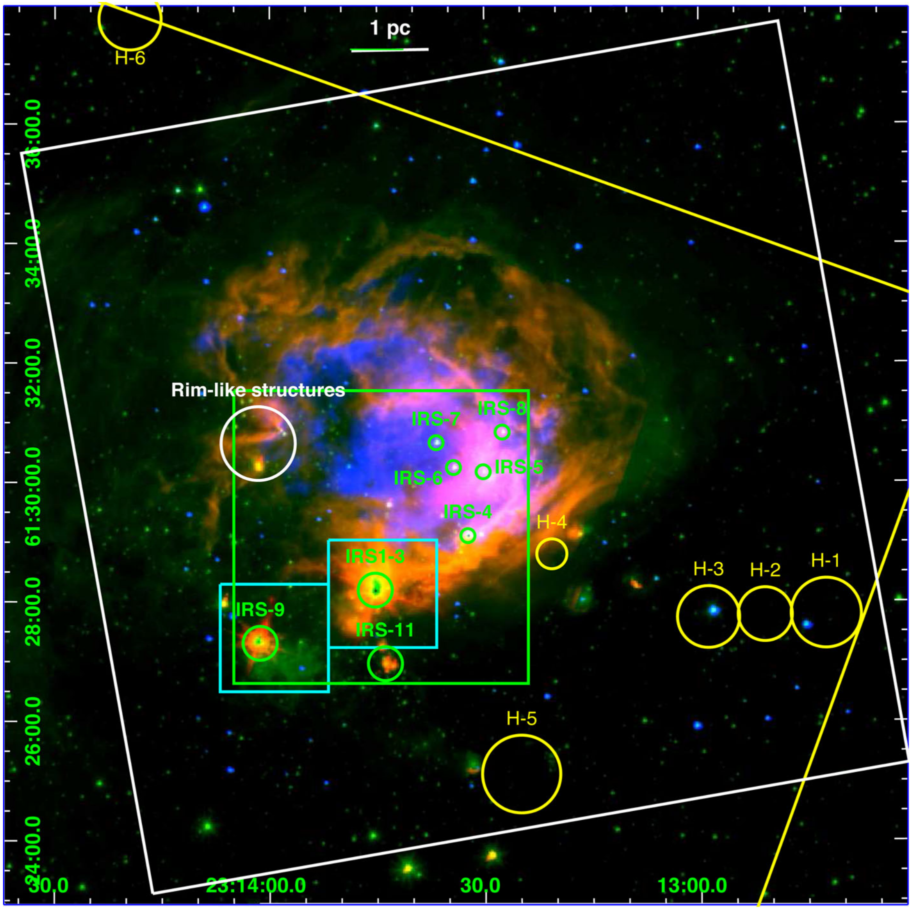

Figure 1. Colour-composite image obtained using the Hα (blue), 3.6 μm (green) and 8.0 μm (red) images for an area of ∼15 × 15 arcmin^2 around NGC 7538. The white box represents the region covered in the optical survey. The region below the slightly horizontal yellow line and westwards of the slightly vertical yellow line represents the area covered in the *Chandra* X-ray survey. The green and cyan boxes represent the areas covered by the NIR surveys of Ojha et al. (2004b) and Mallick et al. (2014), respectively. The positions of various IR sources (IRS 1–11), rim-like structures and *Herschel*-identified massive SFRs (H1–H6) are also shown. The *x*-axis and *y*-axis are the right ascension and declination, respectively, in the J2000 epoch.

hydrodynamic simulations of star formation, including feedback from O-type stars, found that these observational markers do not improve significantly the chances of correctly identifying a given star as triggered, therefore they urge caution in interpreting observations of star formation near feedback-driven structures in terms of triggering. Of course, systems where many putative triggering indicators can be satisfied simultaneously are more likely to be genuine sites of triggering.

NGC 7538 (see Fig. 1), located at a distance of 2.65 kpc (see Appendix A), is an H II region that belongs to the Cas OB2 complex in the Perseus spiral arm (Frieswijk et al. 2008). It contains massive stars in different evolutionary stages: main-sequence (MS) stars with spectral types between O3 and O9 (IRS 6 and IRS 5, Puga et al. 2010), which ionize the H II region NGC 7538; infrared (IR) sources IRS 1 (associated with a disc and an outflow; Pestalozzi, Elitzur & Conway 2009; Sandell et al. 2009), IRS 2 and IRS 3 (Wynn-Williams, Becklin & Neugebauer 1974) located south of NGC 7538 and associated with UCH II regions and with the IR cluster NGC 7538S (Carpenter et al. 1993; Bica, Dutra & Barbuy 2003; Sandell & Wright 2010); and YSOs like IRS 9 and IRS 11 (Werner et al. 1979). Thus, as a SFR associated with an H II region, it is ideally suited for studying the impact of massive stars on the formation of high- and low-mass stars in its surroundings. In this paper, we will study this region in continuation of our efforts to understand the star-formation scenario in such SFRs (Sharma et al. 2007; Pandey et al. 2008, 2013; Jose et al. 2008; Chauhan et al. 2009, 2011; Sharma et al. 2012; Mallick et al. 2012; Jose et al. 2013).

The NGC 7538 region has been studied by Ojha et al. (2004b) using near-infrared (NIR) observations centred at IRS 1–3 (see Fig. 1), along with radio continuum observations at 1280 MHz. They identified YSOs and classified them according to their evolutionary stages using NIR two-colour diagrams (TCDs) and generated the K_s-band luminosity function to discuss the age sequence and mass spectrum of the YSOs in the region. They discerned several substructures at different evolutionary stages. Using an NIR survey, Balog et al. (2004) found that most of the red sources in this region are concentrated at the southern rim bounding the optical H II region and in the area around the IR sources IRS 1–3. Puga et al. (2010) put an upper limit on the age of the central cluster as 2.2 Myr based on the lifetime of the most massive O3V star (60 M$_\odot$, IRS 6). Using high-spatial-resolution submillimetre maps, Sandell & Sievers (2004) found that the three major centres of star-forming activity (IRS 1–3, IRS 11 and IRS 9) in the NGC 7538 region are connected to each other through filamentary dust ridges. Recently, Mallick et al. (2014) observed in NIR the two comparatively smaller regions of NGC 7538 centred on IRS 1–3 and IRS 9 (see Fig. 1) to study the luminosity function and initial mass function (IMF) of these regions. They complemented their deep NIR observations with X-ray, radio and molecular line observations to study the stellar population, ionized gas characteristics and dense molecular gas morphology in the region. Recently, Chavarría et al. (2014) presented homogeneous IR and molecular data to study the spatial distribution of YSOs and the properties of their clustering and correlation with the surrounding molecular cloud structures. They compared these properties of this massive SFR with those of low-mass SFRs. However, they could not reach any concrete conclusion about the triggering mechanism due to the lack of the investigation of the time causality between the expansion of the H II region and the age of the newly formed stars.

Most of the previous studies on star formation in this region concentrated mainly on the IRS 1–11 region directly associated with NGC 7538. In the present work, we will revisit this region, but not only to study a wider area but also to make use of deep optical data of our own along with the multiwavelength archival data sets from various surveys (*Chandra*, *Spitzer* and 2MASS). Whereas previous studies neither derived the physical parameters (ages and masses) of the individual YSOs nor checked for their association with the NGC 7538 region, we have done so and present a catalogue of YSOs containing this information. For some of them, spectral energy distribution (SED) fitting analyses have been applied. The spatial distribution of these YSOs, along with those of the mid-infrared (MIR) and radio emission, and the mass function (MF), will be used to constrain the star-formation history in the region.

The rest of this paper is organized as follows. In Section 2, we describe the optical and archival data sets. In Section 3, we identify YSOs, catalogue them according to their evolutionary stages and derive their physical parameters. The X-ray spectral analysis of the YSOs is also explained in this section. All of these analyses are discussed in Section 4 and the conclusions are summarized in Section 5.

2 OBSERVATION AND DATA REDUCTION

2.1 Optical data

The CCD $UBV(RI)_c$ and Hα + continuum photometric data of the NGC 7538 region, centred at α_{J2000}: $23^h13^m38^s$, δ_{J2000}: $+61°31'23''$ ($l = 111.548°$ and $b = 0.832°$), were acquired on 2004 November 6 and 7 and 2005 October 25, respectively, using the 2048 × 2048 pixel^2 CCD camera mounted on the f/13 Cassegrain focus of the 104-cm Sampurnanand telescope of the Aryabhatta Research Institute of Observational Sciences (ARIES), Nainital, India. In this setup, each pixel of the CCD corresponds to 0.37 arcsec and the entire chip covers a field of ~13 × 13 arcmin^2 on the sky. To improve the signal-to-noise ratio (SNR), the observations were carried out in the binning mode of 2 × 2 pixels. The read-out noise and gain of the CCD are 5.3 e^- and 10 e^- per ADU respectively. The average full widths at half-maximum of the star images were ~2 arcsec. The broad-band $UBV(RI)_c$ observations of the NGC 7538 region were standardized by observing stars in the SA95 field (Landolt 1992) centred on SA 112 (α_{J2000}: $3^h53^m40^s$, δ_{J2000}: $-0°0'54''$) on 2004 November 6. A reference field of ~13 × 13 arcmin^2 located about 10 arcmin south-west of the NGC 7538 region was also observed to estimate the contamination due to foreground and background field stars on 2005 November 30 in VI_c. This reference field was standardized using the stars common with the NGC 7538 region. A log of the observations is given in Table 1. In Fig. 1, we show the observed region (white box) on the colour-composite image of NGC 7538 obtained by combining the Hα (blue), 3.6 µm (green), and 8.0 µm (red) images.

Table 1. Log of optical observations with the 104-cm Sampurnanand Telescope, Nainital.

Date of observations/ Filter	Exposure (s) × number of frames
	NGC 7538
2004 November 6	
U	300 × 4
B	180 × 4, 60 × 3
V	60 × 4
R_c	30 × 4
I_c	30 × 4
2004 November 7	
U	900 × 3
B	600 × 3
V	600 × 3
R_c	300 × 4
I_c	300 × 4
2005 October 25	
Hα	900 × 2, 300 × 3
Continuum	900 × 1, 300 × 1
	Reference field
2005 November 30	
V	600 × 3
I_c	300 × 3

Initial processing of the data frames was done using the IRAF[1] and ESO-MIDAS[2] data reduction packages. Photometry of the cleaned frames was carried out using the DAOPHOT-II software (Stetson 1987). The point spread function (PSF) was obtained for each frame using several uncontaminated stars. Magnitudes obtained from different frames were averaged. When brighter stars were saturated on deep exposure frames, their magnitudes were taken from short exposure frames. We used the DAOGROW program to construct the aperture growth curve required for determining the difference between the aperture and PSF magnitudes.

Calibration of the instrumental magnitudes to the standard system was done using the procedures outlined by Stetson (1992). The calibration equations derived by the least-squares linear regression are as follows:

$$u = U + (7.178 \pm 0.029) - (0.035 \pm 0.039)(U - B) + (0.467 \pm 0.046)X,$$

$$b = B + (4.771 \pm 0.027) - (0.037 \pm 0.028)(B - V) + (0.255 \pm 0.025)X,$$

$$v = V + (4.274 \pm 0.007) - (0.025 \pm 0.005)(V - I_c) + (0.143 \pm 0.005)X,$$

$$r_c = R_c + (4.169 \pm 0.005) - (0.028 \pm 0.009)(V - R_c) + (0.102 \pm 0.003)X,$$

---

[1] IRAF is distributed by the National Optical Astronomy Observatories, USA.

[2] ESO-MIDAS is developed and maintained by the European Southern Observatory.

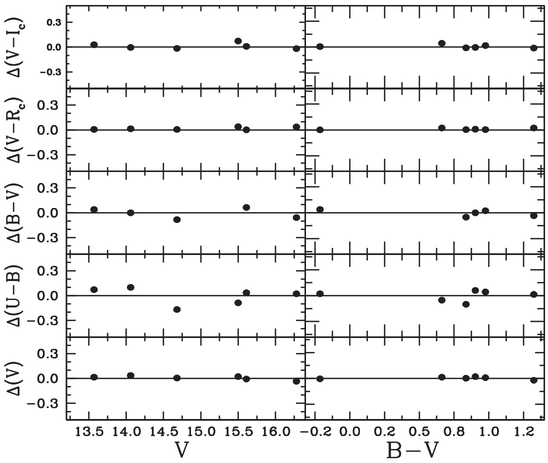

Figure 2. Differences between standard and transformed magnitudes and colours of standard stars plotted against the standard V magnitude and $(B - V)$ colour.

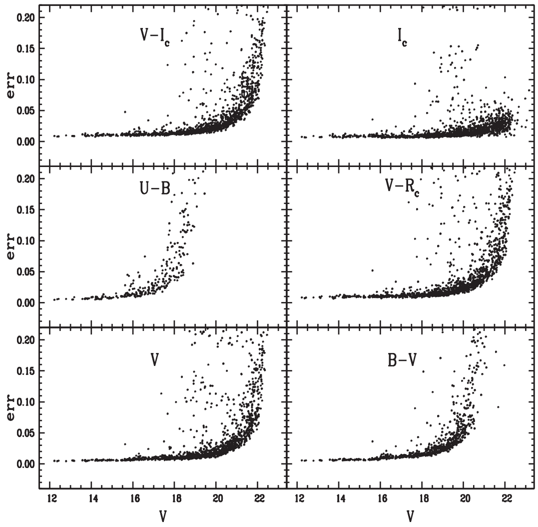

Figure 3. DAOPHOT errors in magnitudes and colours as a function of V magnitude.

$$i_c = I_c + (4.611 \pm 0.011) + (0.022 \pm 0.008)(V - I_c)$$
$$+ (0.072 \pm 0.008)X$$

where U, B, V, R_c and I_c are the standard magnitudes and u, b, v, r_c and i_c are the instrumental aperture magnitudes normalized for 1 s of exposure time and X is the airmass. We have ignored the second-order colour-correction terms as they are generally small in comparison to other errors present in the photometric data reduction. Fig. 2 shows the standardization residual, Δ, between standard and transformed V magnitudes and $(U - B)$, $(B - V)$, $(V - R_c)$ and $(V - I_c)$ colours of the standard stars as a function of V magnitude and $(B - V)$ colour. As can be seen from the figure, the residuals do not show any trends with colour or magnitude. The typical DAOPHOT errors in magnitude and colour as a function of V magnitude are shown in Fig. 3. It can be seen that, in the V band, the errors become large ($\geq$0.1 mag) for stars fainter than $V \simeq 22$ mag, so the measurements beyond this magnitude are not reliable. In total, 969 sources, with detection at least in the V and I_c bands and errors less than 0.1 mag, were identified in this study.

2.2 Grism slitless spectroscopy

Slitless grism spectroscopy has also been carried out for the NGC 7538 region in a search for Hα emission stars. The observations were made with the Himalayan Faint Object Spectrograph Camera (HFOSC) on the 2-m Himalayan Chandra Telescope (HCT) of the Indian Astronomical Observatory (IAO), Hanle, India, on 2004 September 21. A combination of a wide Hα interference filter (6300–6740 Å) and grism 5 (5200–10 300 Å) of HFOSC was used without a slit. The central 2048 × 2048 pixels of the 2048 × 4096 CCD was used for data acquisition. The pixel size is 15 µm with an image scale of 0.297 arcsec pixel^{-1}. The resolution of the spectra is 870. We secured three spectroscopic frames of 5-min and 1-min exposure each with the grism in, as well as three direct frames of 1-min exposure each with the grism out. The seeing size at the time of the observations was ≃2 arcsec.

2.3 Archival data

2.3.1 Chandra *X-ray data*

The NGC 7538 region was observed by the *Chandra* X-ray Observatory on 2005 March 25 (see Fig. 1) centred at $\alpha_{\rm J2000}$: 23$^{\rm h}$13$^{\rm m}$47.8$^{\rm s}$, $\delta_{\rm J2000}$: +61°28′15.5″. The satellite roll angle (i.e. the orientation of the CCD array relative to the north–south direction) during the observations was 19.2°. Exposures of 30 ks were obtained in the very faint data mode with a 3.2 s frame time using the ACIS-I imaging array as the primary detector. ACIS-I consists of four front-illuminated 1024 × 1024 CCDs with a pixel size of 0.492 arcsec and a combined field of view (FOV) of ∼17 × 17 arcmin^2. The region of NGC 7538 observed by *Chandra* is shown in Fig. 1. More detailed information on *Chandra* and its instrumentation can be found in the *Chandra* Proposer's Guide.[3] Tsujimoto et al. (2005) used this data and presented a preliminary report indicating 180 X-ray sources in this region. 123 of them have 2MASS NIR counterparts. They studied IR sources in this region and found that IRS 2, 4, 5, 6, 9 and 11 are bright in X-ray and have soft X-ray spectra like early-type field stars. IRS 7 and 8 were identified as foreground stars due to the absence of X-ray, and IRS 1 and IRS 2 were not detected probably due to high extinction. Recently, Mallick et al. (2014) reported 27 sources with NIR counterparts in the IRS 1–3 and IRS 9 regions (see Fig. 1).

In this study, X-ray data will be used to study the X-ray properties of the YSOs. We have used the CIAO 4.8 data analysis software in combination with the *Chandra* calibration data base CALDB v.4.7.1 to reduce the X-ray data. The light curves from on-chip background regions were inspected for possible large background fluctuations that may have resulted from solar flares; however, we did not find any such fluctuations. After filtering the data for the energy band 0.5 to 8.0 keV, the time-integrated background was found to be 0.06 counts arcsec^{-2}. Source detection was then performed with the Palermo wavelet detection code, PWDETECT (Damiani et al. 1997).[4] It analyses the data at different spatial scales, allowing the detection of both point-like and moderately extended sources, and efficiently resolving close pairs. The most important input parameter for this code is the detection threshold, which we estimated from the relationship between the background level and expected number of spurious detections due to Poisson noise (for details, see Damiani et al. 1997). The background level was determined with the

---

[3] See http://asc.harvard.edu/proposer/POG

[4] http://www.astropa.unipa.it/progetti_ricerca/PWDetect/

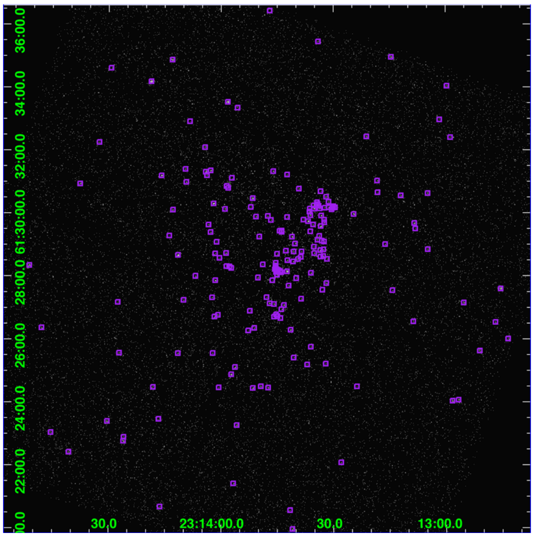

Figure 4. X-ray image obtained from the *Chandra* observations. The identified point sources are shown by purple squares. The *x*-axis and *y*-axis are the right ascension and declination in the J2000 epoch.

BACKGROUND command of XIMAGE. After filtering events in the energy band 0.5–8.0 keV, the ACIS-I observations comprise a total of about 56 000 counts. This background level translates into a SNR threshold of 5.0 if we accept one spurious detection in the FOV, or into SNR 4.6 if we accept 10 spurious detections. The first choice results in the detection of 158 sources, whereas the second detects 193 sources. We decided to adopt the second criterion; however, we manually rejected three sources because they were detected either in the CCD gaps or twice. Finally, 190 X-ray point sources were adopted for further analyses. The locations of these 190 X-ray point sources are shown in Fig. 4 overlaid on the *Chandra* X-ray image.

2.3.2 Spitzer *and 2MASS IR data*

This region was observed by the *Spitzer* space-based telescope on 2006 August 14 (PI: Giovanni Fazio; program ID: 30784) with the Infrared Array Camera (IRAC). These images have been mosaicked to create a 15 × 15 arcmin^2 FOV (see Fig. 1) in all IRAC bands using the MOPEX software provided by the *Spitzer* Science Center. It contains the common area observed in the optical and X-ray wavelengths. These mosaicked images were used to make a colour-composite image of this region (see Fig. 1).

Ojha et al. (2004b) made NIR observations in a 5 × 5 arcmin^2 FOV near IRS 1–3 (see Fig. 1) using the 2.2-m University of Hawaii telescope. The NIR survey has 10σ limiting magnitudes of 19.5, 18.4 and 17.3 in the J, H and K_s bands, respectively. Comparatively smaller regions (1.8 × 1.8 arcmin^2 FOV) centred on IRS 1–3 and IRS 9 (see Fig. 1) were observed using the 8.2-m Subaru telescope by Mallick et al. (2014) in the J, H and K bands. The 10σ limiting magnitudes for these observations were ∼22, 21 and 20 in the J, H and K bands, respectively. Also, recently, Chavarría et al. (2014) compiled J and K data (up to $K \sim 17.5$ mag) in the widest FOV of 20 × 20 arcmin^2 in the NGC 7538 region using the 2.1-m telescope at Kitt Peak National Observatory. These authors published YSO catalogues, which are merged together to form a combined catalogue of YSOs (see Section 3.1.2) in the present study.

We also used the 2MASS Point Source Catalog (PSC) (Cutri et al. 2003) for NIR (JHK_s) photometry in the NGC 7538 region. This catalogue is reported to be 99 per cent complete down to the limiting magnitudes of 15.8, 15.1 and 14.3 in the J, H and K_s bands, respectively.[5] We selected only those sources that have a NIR photometric accuracy <0.2 mag and detection in at least the H and K_s bands.

3 ANALYSIS AND RESULTS

3.1 Identification of YSOs

YSOs are usually grouped into the evolutionary classes 0, I, II and III, which represent in-falling protostars, evolved protostars, classical T-Tauri stars (CTTSs) and weak-line T-Tauri stars (WTTSs), respectively (see Feigelson & Montmerle 1999). Class 0 YSOs are so deeply buried inside the molecular clouds that they are not visible at optical or NIR wavelengths, whereas class I's are characterized by the growth of an accretion disc surrounded by an envelope and are visible in IR and occasionally in optical if viewed in the pole-on direction (Nisini et al. 2005; White et al. 2007; Williams & Cieza 2011). The CTTSs feature discs from which the material is accreted, and line emission, e.g. in Hα, can be seen due to this accreting material. These discs can also be probed through their IR excess (over the normal stellar photospheres). WTTSs, in contrast, have little or no disc material left and hence have no strong Hα emission and IR excess. As the level of X-ray emission of pre-main-sequence (PMS) stars is higher than that of MS stars (e.g. Feigelson & Montmerle 1999; Feigelson et al. 2002; Favata & Micela 2003; Güdel 2004; Caramazza et al. 2012), X-ray observations provide a very efficient means of selecting WTTSs associated with the SFRs, which might be missed in surveys based only on Hα emission and/or IR excess emission. Below, we report the identification of YSOs based on their Hα, IR and/or X-ray emission.

3.1.1 Hα emission

Stars with Hα emission in a SFR are considered as PMS stars or candidates. The strength of the emission (expressed by equivalent width or EW$_{\mathrm{H}\alpha}$) could be a direct indicator of their evolutionary stage. The conventional distinction between CTTSs and WTTSs is $\mathrm{EW}_{\mathrm{H}\alpha} = 10$ Å and it is greater for the former (see Herbig & Bell 1988).

Slitless grism frames were visually inspected to identify stars with Hα enhancement. Then the EW$_{\mathrm{H}\alpha}$ of these stars was estimated using the APALL task of IRAF. EWs in pixels are converted into angstroms by multiplying by 3.8, as has been calculated for grism 5 having resolution $R = 870$ and assuming sampling of 2 pixels.[6] We have identified six Hα emission stars spectroscopically and their position and EW$_{\mathrm{H}\alpha}$ are given in Table 2. Based on the value of EWs, three each were classified as class II and class III sources, respectively.

To identify Hα emission stars, we also used narrow-band Hα photometry based on its excess emission. In the study of NGC 6383, Rauw, Manfroid & De Becker (2010) found that the Hα EW of 10 Å corresponds to an (R_c − Hα) index of 0.24 ± 0.04 mag above the MS relation introduced by Sung et al. (1997).

In the present study, we used this condition to identify Hα emission stars and classified them as class II sources. Since our Hα photometry is not calibrated, to compare this Hα magnitude to that of Sung et al. (1997), we estimated the zero-point by comparing visually the observed (R_c − Hα) and dereddened ($V - I_c$) with the

---

[5] http://tdc-www.harvard.edu/catalogs/tmpsc.html

[6] http://www.iiap.res.in/iao/hfosc.html

Table 2. Hα emission stars identified by grism spectroscopy.

ID	$\alpha_{\rm J2000}$ ($^{\rm h}$:$^{\rm m}$:$^{\rm s}$)	$\delta_{\rm J2000}$ ($^{\circ}$:$'$:$''$)	EW (Hα) (Å)
G1	23:13:16.66	+61:28:01.4	9.9
G2	23:13:32.75	+61:27:49.7	91.2
G3	23:13:56.36	+61:25:06.9	3.0
G4	23:14:06.64	+61:27:57.7	35.0
G5	23:14:13.04	+61:34:52.4	8.4
G6	23:14:13.38	+61:31:46.6	10.6

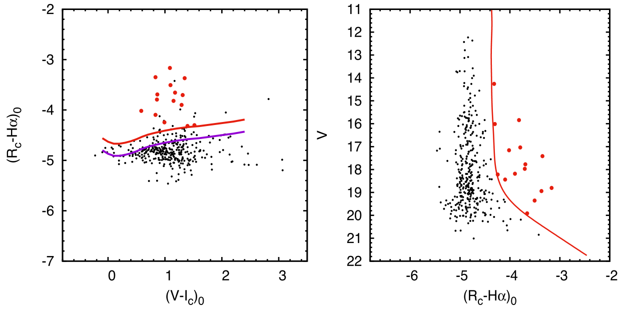

Figure 5. Left: $(R_c - {\rm H}\,\alpha)_0$ index is shown as a function of $(V - I_c)_0$ colour. The blue curve indicates the relation for MS stars as taken from Sung, Bessell & Lee (1997) and reddened for $A_V = 2.3$ mag (see Appendix A). The red curve yields the thresholds for Hα emitter candidates (see Section 3.1.1). Right: V versus $(R_c - {\rm H}\,\alpha)_0$ CMD. The solid curve demarcates the Hα emitter candidates from MS stars. The red dots represent selected Hα emitting candidates.

$(R_c - {\rm H}\,\alpha)_0$ versus $(V - I_c)_0$ relation of emission-free MS stars as determined by Sung et al. (1997) for the NGC 2264 region. We have to subtract 3.85 mag from the observed values to obtain the $(R_c - {\rm H}\,\alpha)$ index in the Sung et al. (1997) system. The $(V - I_c)$ colour is dereddened by the minimum extinction value derived in Appendix A [i.e. $E(B - V)_{\rm min} = 0.75$ mag and $R_V = 2.82$]. In the left-hand panel of Fig. 5, we have plotted the $(R_c - {\rm H}\,\alpha)_0$ versus $(V - I_c)_0$ distribution of all the stars along with the MS relation (blue curve) given by Sung et al. (1997). All the sources above the red curve (0.24 mag above the MS relation, see Sung et al. 1997) are assumed as Hα excess emission sources of the class II evolutionary stage. Since there is a large scatter in the distribution in the left-hand panel of Fig. 5, there may be some false identifications of Hα emitters.

To minimize false detections, we introduced another selection criterion using the V versus $(R_c - {\rm H}\,\alpha)_0$ colour–magnitude diagram (CMD; see Fig. 5 right-hand panel). We define an envelope that contains MS stars, keeping in mind its broadening at faint magnitudes due to large photometric errors and the possible presence of binaries, field stars etc. (Phelps & Janes 1994). The stars that have $(R_c - {\rm H}\,\alpha)_0 - \sigma_{(R_c - {\rm H}\,\alpha)_0}$ larger than that of the envelope of the MS can be safely assumed as probable Hα emitters (Kumar et al. 2014). Our final criterion for photometrically selected Hα emitters is to satisfy both of the above conditions. 15 sources (red dots in Fig. 5) were identified as Hα emitting YSOs and were categorized as class II YSOs. None of them were identified through grism spectroscopy.

In total, 21 stars were classified as YSOs (three as class III and 18 as class II) based on Hα spectroscopy and photometry.

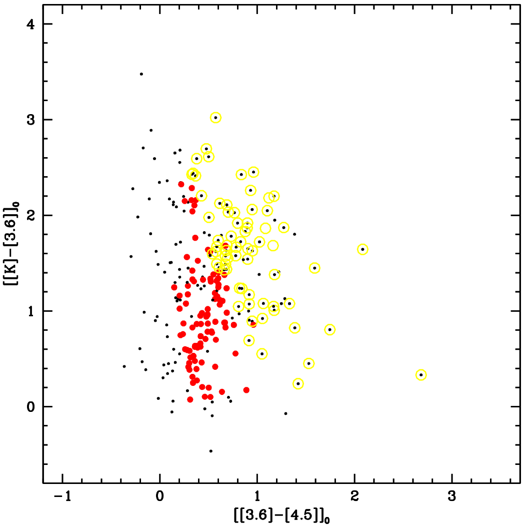

Figure 6. $[[K] - [3.6]]_0$ versus $[[3.6] - [4.5]]_0$ TCD for those YSOs identified by Chavarría et al. (2014) that lack detection at either 5.8 or 8.0 µm but have NIR detection in the K band (black dots). The YSOs classified as class I and class II, based on the colour criteria of Gutermuth et al. (2009), are shown using yellow circles and red dots, respectively.

3.1.2 IR emission

Recently, Chavarría et al. (2014) identified 562 YSOs in a 15×15 arcmin^2 FOV of the NGC 7538 region based on NIR/MIR excess emission. They classified 234 YSOs that have detections in all four IRAC bands based on the value of the slopes ($\alpha_{\rm IRAC}$) of their SEDs. We further used the $[[3.6] - [4.5]]_0$ versus $[[K] - [3.6]]_0$ TCD (for details, see Gutermuth et al. 2009) to classify the remaining YSOs. YSOs having $[J - H]$ colour $\geq$0.6 mag and lying above the CTTS locus or its extension are traced back to the CTTS locus or its extension to get their intrinsic colours. For YSOs that lack J band photometry, baseline colours in the $[H - K]$ versus $[[3.6] - [4.5]]$ colour–colour space YSO locus, as measured by Gutermuth et al. (2005), are used to get their intrinsic colours. 43 class I and 108 class II sources were classified using their location in the above mentioned TCD and are shown as yellow circles and red dots, respectively, in Fig. 6. For those YSOs that are not detected in the IRAC bands but have NIR (JHK) detections and have $(J - H) > 0.6$ mag (13 sources), we used the classical NIR TCDs (see Ojha et al. 2004b; Sharma et al. 2012) to classify them. Finally, out of 562 YSOs, 239 (234 IRAC four-band sources plus five MIPS sources) were classified by Chavarría et al. (2014) and 164 are classified in this study. The remaining 159 YSOs could not be classified as either they have no IRAC detections and $(J - H) < 0.6$ mag or they do not fall at the location of class I/II YSOs in the IRAC $[[3.6] - [4.5]]_0$ versus $[[K] - [3.6]]_0$ TCD.

Ojha et al. (2004b) studied the NGC 7538 region and identified and classified 286 YSOs (18 class I and 268 class II YSOs) based on their excess emission in IR using their location in the NIR TCD (e.g. Fig. 7). The solid and thick black dashed curves in Fig. 7 represent the unreddened MS and giant branch (Bessell & Brett 1988), respectively. The dotted blue line indicates the locus of unreddened CTTSs (Meyer, Calvet & Hillenbrand 1997). The parallel dashed red lines are the reddening lines drawn from the tip (spectral type M4) of the giant branch (upper reddening line), from the base (spectral type A0) of the MS branch (middle reddening line) and from the tip of the intrinsic CTTS line (lower reddening line). The extinction ratios $A_J/A_V = 0.265$, $A_H/A_V = 0.155$ and $A_K/A_V = 0.090$ have

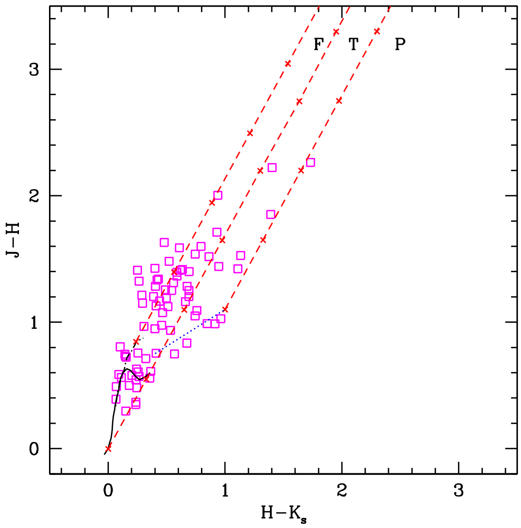

Figure 7. NIR TCD for the sources having X-ray counterparts (purple squares) in the NGC 7538 region. The continuous and thick black dashed curves represent the dereddened MS and giant branches (Bessell & Brett 1988), respectively. The dotted blue line indicates the locus of dereddened CTTSs (Meyer et al. 1997). The parallel red dashed lines are the reddening lines drawn from the tip (spectral type M4) of the giant branch (left reddening line), from the base (spectral type A0) of the MS branch (middle reddening line) and from the tip of the intrinsic CTTS line (right reddening line). The crosses on the reddening lines show an increment of $A_V = 5$ mag.

been taken from Cohen et al. (1981). These extinction ratios are for the normal Galactic medium (i.e. $R_V = 3.1$), since for $\lambda > \lambda_I$, the reddening law can be taken as a universal quantity (Cardelli, Clayton & Mathis 1989; He et al. 1995).

The sources can be classified according to the three regions in this diagram (see Ojha et al. 2004a). F sources are between the upper and middle reddening lines and are considered to be either field stars (MS stars or giants) or class III sources and class II sources with small NIR excess. T sources are between the middle and lower reddening lines. These sources are considered to be mostly CTTSs (or class II objects) with a large NIR excess. There may be an overlap of Herbig Ae/Be stars in the T region (Hillenbrand et al. 1992). P sources are those located in the region red-ward of the lower reddening line and are most likely class I objects (protostellar-like objects; Ojha et al. 2004a).

Most recently, Mallick et al. (2014) also identified and classified 168 YSOs (24 class I and 144 class II) similarly in the IRS 1–3 region. We combined these two NIR data sets with a match radius of 1 arcsec and catalogued 408 YSOs (40 class I and 368 class II; 46 were in both catalogues). After combining this catalogue with that of Chavarría et al. (2014, 562 YSOs) with the same match radius of 1 arcsec, we compiled altogether 890 YSOs (80 YSOs were in both catalogues) in the selected region of NGC 7538. 169, 569 and three are class I, class II and class III objects, respectively. Details are given in Table 3.

Table 3. Sample table containing information for 890 catalogued YSOs from Ojha et al. (2004b), Chavarría et al. (2014) and Mallick et al. (2014) in the NGC 7538 region. The complete table is available in electronic form only.

ID^a	$\alpha_{(2000)}$ ($^{\rm h}$:$^{\rm m}$:$^{\rm s}$)	$\delta_{(2000)}$ (°:′:″)	Class^b	Class^c	Class^d	Class^e
C_{2361}	23:12:34.40	+61:27:11.3	II	–	–	–
C_{2362}	23:12:37.42	+61:36:16.2	–	–	–	–
C_{2363}	23:12:40.88	+61:24:56.5	II	–	–	–
C_{2364}	23:12:40.88	+61:31:38.8	II	–	–	–
C_{2365}	23:12:41.18	+61:28:02.1	II	–	–	–

Notes. ^{a}O, C and M are YSOs catalogued in Ojha et al. (2004b), Chavarría et al. (2014) and Mallick et al. (2014), respectively. ^{b}Classification by Chavarría et al. (2014) based on IRAC SED slope. ^{c}Classification by IRAC TCDs. ^{d}Classification by Ojha et al. (2004b) and Mallick et al. (2014) through NIR TCDs. ^{e}Classification by Hα and X-ray emission, i.e. I, II, III or comment. If comment is 7, Hα emission star (spectroscopy), if comment is 8, Hα emission star (photometry), and if comment is 9, X-ray emitting star.

3.1.3 X-ray emission

The sample of YSOs selected based on their IR excess may be incomplete because the circumstellar discs in young stars may disappear on time-scales of just a few million years (see Briceño et al. 2007). Recent studies of a few SFRs reveal that disc fraction decreases with age of the region, e.g. Sh 2-311: 35 per cent disc fraction, age 4 Myr, distance 5 kpc (Yadav et al. 2016); NGC 2282: 58 per cent disc fraction, age 2–5 Myr, distance 1.65 kpc (Dutta et al. 2015); W3-AFGL333: 50–60 per cent disc fraction, age 2 Myr, distance 2 kpc (Jose et al. 2016). Since the average age of the YSOs in the NGC 7538 region is 1.4 Myr (see Section 4.1), we would expect that less than 40 per cent of the YSOs do not show excess emission in NIR/MIR (Haisch, Lada & Lada 2001; Hernández et al. 2008).

Since the X-ray detection method is sensitive also to young stars that have already dispersed their circumstellar discs (Preibisch et al. 2011), we considered X-ray emitting stars and classified them according to their evolutionary stages using the classical NIR TCDs (Jose et al. 2008; Pandey et al. 2008; Sharma et al. 2012; Kumar et al. 2014).

In Fig. 7, we have plotted the NIR TCD for the X-ray counterparts. Since none of the previous studies on the NGC 7538 region (see Ojha et al. 2004b; Mallick et al. 2014; Chavarría et al. 2014) have published their deep photometric catalogues online, we used 2MASS data to find the NIR counterparts of the X-ray sources. The *Chandra* on-axis PSF is 0.5 arcsec and it degrades at large off-axis angles (see e.g. Getman et al. 2005; Broos et al. 2010). So we used an optimal matching radius of 1 arcsec to determine the 2MASS NIR counterparts of the X-ray sources. This size of the matching radius is established well in other studies as well (see e.g. Feigelson et al. 2002; Wang et al. 2007). 90 of the X-ray emitting sources have 2MASS NIR counterparts in the selected region (15 × 15 arcmin^2 FOV) of NGC 7538. All the 2MASS magnitudes and colours have been converted into the California Institute of Technology (CIT) system.[7] All the curves and lines are also in the CIT system. The sources falling in the F region and above the extension of the intrinsic CTTS locus as well as the sources having $(J - H) \geq 0.6$ and lying to the left of the upper reddening line are assigned as WTTSs/class III sources (45 sources) (see e.g. Jose et al. 2008; Pandey et al. 2008; Sharma et al. 2012; Kumar et al. 2014). The X-ray counterparts in the T (12 sources) and P (one source) regions are classified as class II and class I sources, respectively.

---

[7] http://www.astro.caltech.edu/~jmc/2mass/v3/transformations/

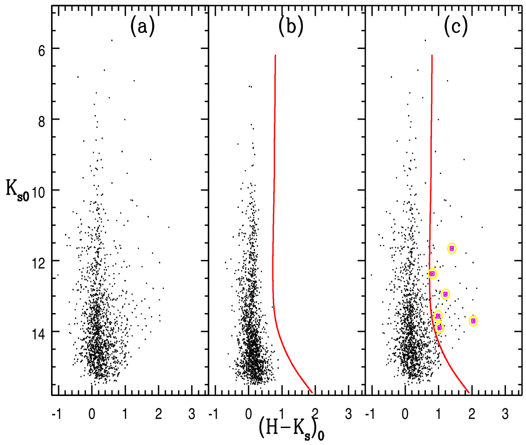

Figure 8. $K_{s0}/(H-K_s)_0$ CMD for (a) stars in the NGC 7538 region, (b) stars in the reference field and (c) identified X-ray emitting IR excess stars (purple squares inside yellow circles). The thick red line demarcates the X-ray emitting IR excess stars from MS stars.

16 X-ray sources do not have *J*-band data. These sources were classified by comparing the dereddened $K_{s0}/(H-K_s)_0$ CMD of the studied region with that of the reference field, which has an equal area (see Fig. 8). This scheme has been explained in detail by Kumar et al. (2014). The amounts of reddening and extinction were estimated on the extinction map obtained using the NIR TCD. Briefly, the stars having $(J-H)$ colour $\geq$0.6 mag and lying above the CTTS locus or its extension were traced back to the CTTS locus or its extension to get the amount of reddening. Once we have the amount of reddening for individual stars, we can generate extinction maps for the target and field regions. The extinction maps were then used to deredden the remaining stars. The solid red curve in Fig. 8 represents the outer boundary of the field star distribution in the CMD taking into account the scatter due to photometric errors and variations in the A_V values (see for details Kumar et al. 2014). All the stars having a colour $(H-K)_0-\sigma_{(H-K)_0}$ larger than the red cut-off curve in the studied region are believed to have excess emission in the K_s band and can be presumed as class I YSOs (see also Ojha et al. 2004b; Mallick et al. 2012; Kumar et al. 2014). We have classified six sources without *J*-band detections as class I based on the above criterion.

In total, 64 sources with X-ray emission were classified as YSOs (45 as class III, 12 as class II and seven as class I) based on their positions in the NIR TCD/CMD.

3.1.4 The YSO sample

We cross-identified the YSOs detected in the present survey based on Hα (21 sources, see Section 3.1.1) and X-ray emission (64 sources, see Section 3.1.3) with those that were detected based on excess IR emission and are available in the literature (890 sources, see Section 3.1.2 and Table 3, Ojha et al. 2004b; Mallick et al. 2014; Chavarría et al. 2014), using a search radius of 1 arcsec. We found six Hα and 26 X-ray emitting sources that are also showing excess IR emission, thus we confirmed their identification. The remaining 53 sources (see Table 4) are new additions and have been added to make a catalogue of 943 YSOs altogether in the 15 × 15 arcmin^2 field around NGC 7538. Optical counterparts for 74 of these YSOs were also identified using a search radius of 1 arcsec. The position, magnitude, colour and classification of these YSOs are given in Table 5.

Since the aim of this work is to study the star-formation activities in the NGC 7538 region, information about the individual properties of the YSOs is vital. These are derived using the SED fitting analysis (see Section 3.2.1). The SEDs of YSOs can be generated using the multiwavelength data (i.e. optical to MIR) under the condition that a minimum of five data points should be available. Out of 943 YSOs, 463 satisfy this criterion and, therefore, are used in the further analysis. The evolutionary classes of most of these YSOs were defined based on available data sets. First, they were classified based on $\alpha_{\rm IRAC}$ (see Chavarría et al. 2014). Those that do not have $\alpha_{\rm IRAC}$ were then classified based on the MIR + NIR TCD. If IRAC data were not available, then the NIR TCD classification scheme was used (see Section 3.1.2). Finally, the YSOs newly identified based on their X-ray and Hα emission (see Sections 3.1.1 and 3.1.3) were classified based on their IR excess properties and the EWs of the Hα line, respectively.

3.1.5 Source contamination and the completeness of the YSO sample

We have a sample of 419 YSOs for which SEDs can be generated and are associated with the NGC 7538 SFR (see Section 4.1). Our candidate YSOs may be contaminated by IR excess sources such as star-forming galaxies, broad-line active galactic nuclei, unresolved shock emission knots, objects that suffer from polycyclic aromatic hydrocarbon (PAH) emissions etc. that mimic the colours of YSOs. Since we are observing through the Galactic plane, contamination due to galaxies should be negligible (Massi et al. 2015).

To get a statistical estimate of possible galaxy contamination in our YSO sample, we used the Spitzer Wide-area Infrared Extragalactic (SWIRE) catalogue obtained from the observations of the ELAIS N1 field (Rowan-Robinson et al. 2013). SWIRE is a survey of the extragalactic field using the Spitzer-IRAC and MIPS bands and can be used to predict the number of galaxies in a sample of YSOs (Evans et al. 2009). The SWIRE catalogue is resampled for the spatial extent as well as the sensitivity limits of the photometric data in the NGC 7538 region and is also corrected by the average extinction (i.e. $A_V = 11$ mag, see Section 4.1). 17 sources in the SWIRE catalogue could satisfy these criteria. Similarly, out of the 397 YSOs having IRAC photometry, seven can approximately be categorized as obscured AGB stars, as they have a very bright MIR flux, i.e. [4.5] $\leq$ 7.8 mag (see Robitaille et al. 2008). Therefore, the contribution of various contaminants in our YSO sample should be ~6 per cent, which is a small fraction of the total number of YSOs. We also applied the colour–magnitude criteria of Gutermuth et al. (2009) to the YSOs classified by Chavarría et al. (2014) based on their IRAC SEDs, and ~28 per cent of them are matched with the colours of PAH-contaminated apertures, shock emissions, PAH-emitting galaxies and active galactic nuclei. Recently, Jose et al. (2016) also checked the same scheme applied to their sample of YSOs in the W3-AFGL333 region and found that ~38 per cent of class I sources and ~15 per cent of class II sources in their sample were contaminants. However, using our statistical approach, they found only <5 per cent contaminants in their sample of YSOs. Several studies (e.g. Koenig et al. 2008; Rivera-Ingraham et al. 2011; Willis et al. 2013) have noticed that the Gutermuth et al. (2009) criteria for a region at ~2 kpc would likely provide an overestimation of the contamination.

For the above mentioned sample of YSOs with data from various surveys, knowledge of its completeness in terms of mass is

Table 4. Sample table containing information for 53 newly identified YSOs. The J, H and K_s magnitudes and their errors are from the 2MASS PSC. The complete table is available in electronic form only.

ID	$\alpha_{(2000)}$ ($^{\rm h}$:$^{\rm m}$:$^{\rm s}$)	$\delta_{(2000)}$ (°:′:″)	$J \pm \sigma$ (mag)	$H \pm \sigma$ (mag)	$K_s \pm \sigma$ (mag)	Class^a
S_1	23:13:49.12	+61:30:15.4	11.966 ± 0.024	11.120 ± 0.030	10.783 ± 0.019	II(8)
S_2	23:13:29.47	+61:30:38.9	12.447 ± 0.034	11.945 ± 0.039	11.649 ± 0.039	II(8)
S_3	23:13:56.29	+61:25:07.3	13.455 ± 0.031	12.843 ± 0.035	12.553 ± 0.032	III(7)
S_4	23:14:15.91	+61:31:12.1	13.608 ± 0.027	12.843 ± 0.028	12.666 ± 0.023	III(9)
S_5	23:13:31.96	+61:27:47.3	13.697 ± 0.030	12.223 ± 0.032	11.495 ± 0.019	III(9)

Notes. ^{a}Classification by Hα and X-ray emission, i.e. I, II, III or comment. If comment is 7, Hα emission star (spectroscopy), if comment is 8, Hα emission star (photometry), and if comment is 9, X-ray emitting star.

Table 5. Sample table containing information for 74 optically identified YSOs. The age and mass of the YSOs are derived from the optical CMD. IDs are the same as in Tables 3 and 4. The complete table is available in electronic form only.

ID	$V \pm \sigma$ (mag)	$(U-B) \pm \sigma$ (mag)	$(B-V) \pm \sigma$ (mag)	$(V-R_c) \pm \sigma$ (mag)	$(V-I_c) \pm \sigma$ (mag)	Age $\pm \sigma$ (Myr)	Mass $\pm \sigma$ (M$_\odot$)
C_{2833}	12.369 ± 0.004	− 0.047 ± 0.005	0.611 ± 0.005	0.401 ± 0.007	0.806 ± 0.008	0.4 ± 0.1	5.8 ± 0.1
C_{2864}	13.903 ± 0.005	0.676 ± 0.007	0.970 ± 0.006	0.576 ± 0.011	1.077 ± 0.009	1.2 ± 0.1	3.9 ± 0.3
C_{2523}	14.259 ± 0.007	0.081 ± 0.006	1.402 ± 0.008	1.050 ± 0.012	2.251 ± 0.013	0.1 ± 0.1	5.4 ± 0.1
C_{2411}	14.360 ± 0.006	0.016 ± 0.006	0.742 ± 0.006	0.460 ± 0.009	0.950 ± 0.009	2.5 ± 1.9	4.9 ± 0.3

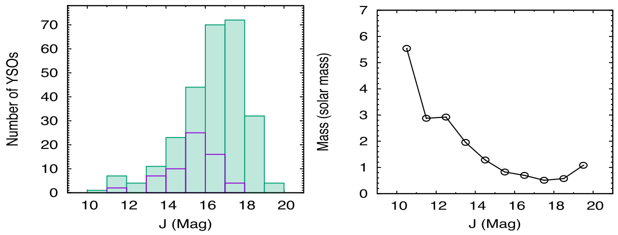

Figure 9. Histogram (green) showing the distribution of the number of YSOs in different J magnitudes (left-hand panel) and the corresponding mass limit of the YSOs (right-hand panel). The blue histogram represents the sample of X-ray emitting YSOs (64) having 2MASS detections.

necessary, but we cannot use the ADDSTAR routine to derive it. Therefore, we instead drew histograms for the numbers of YSOs in different magnitude bins and checked for their peaks. A peak will roughly represent the completeness limit of the data in terms of magnitude (Jose et al. 2013, 2016; Willis et al. 2013; Sharma et al. 2016). Once we know this, the corresponding mass is taken as that of the lowest mass YSO. For example, in Fig. 9 we show the distribution of the numbers of YSOs in different J magnitudes and the corresponding mass limit of the YSOs. The peak of this histogram is between 17 and 18 mag and for this magnitude bin, the corresponding mass is 0.5 M$_\odot$. In this way we found that our data are complete down to 0.5, 0.8, 0.8, 0.8 and 0.6 M$_\odot$ in the J, H, K_s, 3.6 μm and 4.8 μm bands, respectively. Since the sources undetected at 5.8 μm and 8.0 μm were classified based on the 3.6 μm, 4.8 μm, H and K_s band photometry, their completeness limit is not included here. The mass completeness for the YSOs having X-ray and Hα emission will depend on the completeness limit of the photometric data from which they were identified. The completeness limit for the X-ray emitting YSOs (64) is 0.8 M$_\odot$, as inferred from the peak of the blue histogram in Fig. 9. For the Hα emitting sources, the completeness can be approximated as 0.8 M$_\odot$, which is equivalent to that of the optical data. To conclude, we have taken the highest of these, i.e. 0.8 M$_\odot$, as the completeness limit for the detection of the current YSO sample.

3.2 YSO parameters

3.2.1 *From SED analysis*

We constructed SEDs of the YSOs using the grid models and fitting tools of Robitaille et al. (2006, 2007) to characterize them and understand their nature. The models were computed using 20 000 2D radiation transfer calculations based on Monte Carlo from Whitney et al. (2003a,b, 2004) and by adopting several combinations of a central star, a disc, an in-falling envelope and a bipolar cavity in a reasonably large parameter space and with 10 viewing angles (inclinations). The SED fitting tools provide the evolutionary stage and physical parameters, such as mass, age, disc mass, disc accretion rate and stellar temperature of YSOs, and, hence, they are ideal for studying the evolutionary status of YSOs.

We constructed the SEDs of 463 YSOs using the multiwavelength data (optical to MIR wavelengths, i.e. 0.37, 0.44, 0.55, 0.65, 0.80, 1.2, 1.6, 2.2, 3.6, 4.5, 5.8 and 8.0 μm) and with a condition that a minimum of five data points should be available (see Section 3.1.4). The SED fitting tool fits each of the models to the data, with the distance and extinction as free parameters. The distance of the NGC 7538 region is taken as $2.65^{+0.12}_{-0.11}$ kpc (see Appendix A), but the input value ranges for the fitting tool are given with three times the error of the adopted distance, i.e. $2.65 - 0.12 \times 3$ to $2.65 + 0.12 \times 3 = 2.3$ to 3.0 kpc. Since this region is highly nebulous and Ojha et al. (2004b, Fig. 6) detected YSOs up to $A_V = 25$ mag, we varied A_V in a broader range (i.e. from 0 to 30 mag) with three times the errors associated with the foreground A_V value (±2 mag, see Appendix A) and keeping in mind the nebulosity associated with this SFR (see also Samal et al. 2012; Jose et al. 2013; Panwar et al. 2014).

We further set photometric uncertainties of 10 per cent for optical and 20 per cent for both NIR and MIR data. These values are adopted instead of the formal errors in the catalogue to allow a fit without any possible bias caused by underestimating the flux uncertainties. We obtained the physical parameters of the YSOs using the relative probability distribution for the stages of all the well-fitting models. The well-fitting models for each source are defined by

$$\chi^2 - \chi^2_{\rm min} \leq 2N_{\rm data},$$

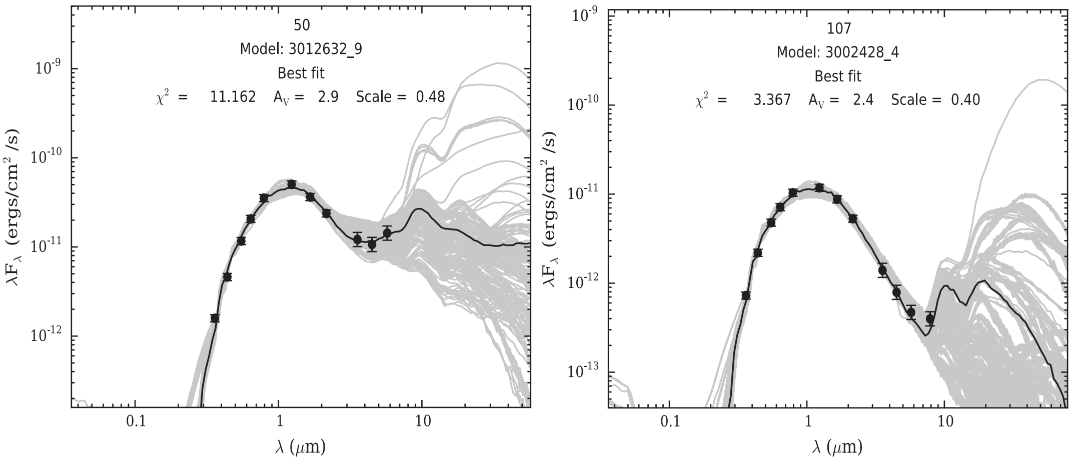

Figure 10. Sample SEDs for class I (left-hand panel) and class II (right-hand panel) sources created by the SED fitting tools of Robitaille et al. (2007). The black curve shows the best fit and the grey curves show the subsequent well fits. The filled circles with error bars denote the input flux values.

where $\chi^2_{\rm min}$ is the goodness-of-fit parameter for the best-fitting model and $N_{\rm data}$ is the number of input data points.

In Fig. 10, we show example SEDs of class I and class II sources, where the solid black curves represent the best fits and the grey curves are the subsequent good fits. As can be seen, the SED of the class I source rises substantially in MIR in comparison to that of the class II source due to its optically thick disc. The sheer number of grey curves in the SED indicates how difficult it was to select a single best-fitting model for these data, which is not surprising given that there are no anchors at long wavelengths. Note that the class I source shown in Fig. 10 was optically detected, which is not usual, but there are also several other cases where such class I sources are detected optically, e.g. Pandey et al. (2013, NGC 1931), Jose et al. (2013, Sh 2-252), Chauhan et al. (2011, W5-East), Ojha et al. (2011, Sh 2-255-257) and Yadav et al. (2016, Sh-2 311). In the present study, five class I sources have optical detections. The optical detection of class I sources can be attributed to their viewing angle (Nisini et al. 2005; White et al. 2007; Williams & Cieza 2011).

Also, some class I and class II sources can exhibit similar SEDs in the *Spitzer* bands (Hartmann et al. 2005; Robitaille et al. 2006; Williams & Cieza 2011). As an example, the models of Whitney et al. (2003a) show that mid-latitude (∼40°)-viewed class I stars have optical and NIR/MIR characteristics like those of more edge-on disc (∼75°) class II stars. The effects of the edge-on disc orientation are most severe for evolutionary diagnostics determined in NIR/MIR, such as the 2–25 μm spectral index (White et al. 2007). A definitive identification of class I sources requires other observations that better constrain the presence of an envelope, such as MIR spectroscopy, far-infrared (FIR) and millimetre photometry, and high-resolution images (Luhman et al. 2010).

From the well-fitting models for each source derived from the SED fitting tool, we calculated the χ^2 weighted model parameters such as A_V, distance, stellar mass and stellar age of each YSO. These are given in Table 6 along with their adopted evolutionary classes (see Section 3.1.4). The error in each parameter is calculated from the standard deviation of all well-fitting parameters.

3.2.2 *From optical colour–magnitude diagram*

By comparing the positions of YSOs in the optical CMD with theoretical isochrones, we can determine their age and mass. In Fig. 11, the $V/(V-I_c)$ CMD has been plotted for all the sources in

Table 6. Sample table containing stellar parameters of 419 selected YSOs derived using the SED fitting analysis. IDs are the same as in Tables 3 and 4. The complete table is available in electronic form only.

ID	$N_{\rm data}$	Class	$\chi^2_{\rm min}$	Distance ± σ (kpc)	A_V ± σ (mag)	Age ± σ (Myr)	Mass ± σ ($M_\odot$)
C_{2361}	6	II	1.7	2.5 ± 0.2	19.8 ± 3.7	0.8 ± 0.9	1.7 ± 1.0
C_{2363}	6	II	3.1	2.6 ± 0.3	18.0 ± 2.6	1.2 ± 1.7	1.1 ± 0.8
C_{2364}	7	II	0.7	2.6 ± 0.3	4.4 ± 1.8	1.5 ± 1.5	1.2 ± 0.7
C_{2365}	6	II	0.6	2.6 ± 0.3	21.2 ± 3.6	1.0 ± 1.4	1.5 ± 0.9

Note. The evolutionary classes of the YSOs are from Tables 3 and 4 (see Section 3.1.4).

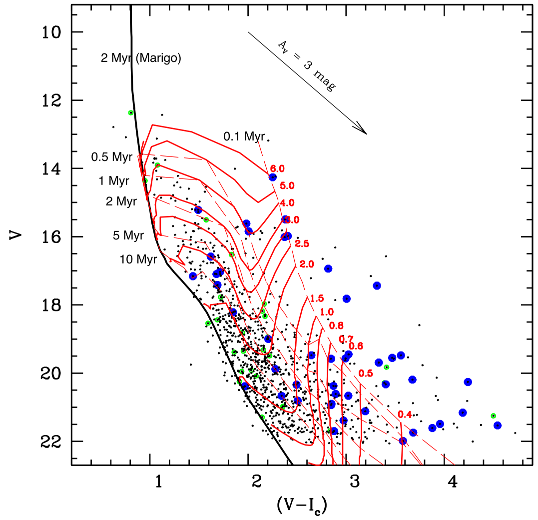

Figure 11. $V/(V-I_c)$ CMD for all the optically detected sources in the NGC 7538 region. Blue dots are identified YSOs and green circles are the sources categorized as non-members of the region (see Section 4.1 for details). The isochrone for 2 Myr from Marigo et al. (2008) (thick black curve) along with the PMS isochrones of 0.1, 0.5, 1, 2, 5 and 10 Myr (red dashed curves) and the evolutionary tracks of different masses (red curves) from Siess et al. (2000) are also shown. All the isochrones and evolutionary tracks are corrected for the distance of 2.65 kpc and reddening $E(B-V) = 0.75$ mag.

the NGC 7538 region along with 74 optically detected YSOs. The post-MS isochrone for 2 Myr calculated by Marigo et al. (2008) (thick black curve) along with the PMS isochrones of 0.1, 0.5, 1, 2, 5 and 10 Myr (red dashed curves) and evolutionary tracks of different masses (red curves) from Siess, Dufour & Forestini (2000) are also shown. These isochrones are corrected for the distance ($2.65^{+0.12}_{-0.11}$ kpc, see Appendix A) and the foreground reddening [$E(B-V)_{\rm min} = 0.75 \pm 0.2$ mag, see Appendix A] of NGC 7538 using the reddening law $R_V = 2.82$ (see Appendix B).

Here, it is highly likely that not all the YSOs are situated on the surface of the associated cloud but embedded in it, where the reddening law is anomalous ($R_V = 3.85$, see Appendix B). Changing the reddening law can affect the derivation of the physical parameters of the YSOs. Therefore, we checked the change in the position of a YSO in the dereddened optical CMD, corrected for the extinction $A_V = 3$ mag (i.e. the average extinction value of the optically detected YSOs, see Section 3.2.1, Table 6) by applying different R_V values. After removing the foreground contribution, the intra-cluster extinction in V and $(V - I_c)$ will be 0.9 and 0.34 mag, respectively, for $R_V = 3.85$, and 0.7 and 0.28 mag, respectively, for $R_V = 2.82$. Therefore, a change in the reddening law will have a marginal effect on the derived physical parameters. However, the amount of intra-cluster reddening can affect the derivation of the ages and masses of the YSOs, if not corrected individually. As we can see from Fig. 11, the reddening vector is almost parallel to the isochrones, but nearly perpendicular to the evolutionary tracks for various masses. This will be nominal in deriving the ages, but can be substantial for the mass estimation.

The ages and masses of the YSOs have been derived from the optical CMD (see Fig. 11) by applying the following procedure. We created an error box around each observed data point using the errors associated with photometry as well as errors associated with estimating the reddening and distance as given in the previous paragraph. 500 random data points were generated using Monte Carlo simulations in this box. The age and mass of each generated point were estimated from the nearest passing isochrone and evolutionary track by Siess et al. (2000). For accuracy, the isochrones and evolutionary tracks were used in a bin size of 0.1 Myr and were interpolated by 2000 points. Finally, we have taken their mean and standard deviation as the final derived values and errors, and these are given in Table 5.

We compare in Fig. 12 the age estimates obtained from the CMD and the SED fitting. The distribution indicates, in general, that there is reasonable agreement between them with a large scatter. We have calculated the linear Pearson correlation coefficient ($r = 0.71$) for this distribution and found that the probability of having no correlation is negligible (i.e. 10^{-6}). The scatter in Fig. 12 may be due to the difference in reddening and extinction corrections to the magnitudes and colours of the YSOs in these two techniques. In the optical CMD, we used a fixed foreground reddening value for all the YSOs, while in the SED fitting, A_V was given as a free parameter in a broad range to deredden the individual YSOs. Therefore, from the CMDs, the very young YSOs, which tend to be deeply embedded in the cloud, may be assigned lower ages than their actual ages.

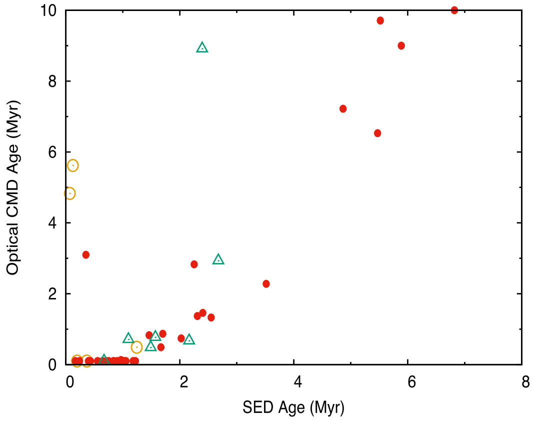

Figure 12. Comparison of the age estimates obtained from the CMD analysis with those from the SED fitting. Yellow open circles, red filled circles and green open triangles represent class I, class II and class III sources, respectively.

3.3 X-ray spectral analysis

The present data contain 190 X-ray emitting sources, of which 91 are classified as YSOs, either based on their location on the NIR TCD/CMD (64, see Section 3.1.3) or because they have a counterpart in an already published list of YSOs (27, see Section 3.1.2). For the X-ray spectral analysis, we selected 21 with more than 35 counts (SNR $>$ 5) in the energy band 0.2–8.0 keV to ensure the minimum quality of the spectral fits.

The spectra of these sources and the background were extracted using the SPECEXTRACT task. The radii of the extracted regions of the sources varied between 5 and 15 arcsec depending on the position of the source detected by the PWDETECT task (see Section 2.3.1) on the detector as well as on its angular separation with respect to the neighbouring X-ray sources. For each source, the background spectrum was obtained from multiple source-free regions chosen according to the source location on the same CCD. The spectra were binned to have a minimum of 5 counts per spectral bin using the GRPPHA task included in FTOOLS.

Finally, a spectral analysis was performed based on the global fitting using the Astrophysical Plasma Emission Code (APEC) version 1.10 modelled by Smith et al. (2001) and implemented in XSPEC version 12.3.0. The plasma model APEC calculates both line and continuum emissivities for a hot optically thin plasma that is in collisional ionization equilibrium. The photoelectric absorption model (photoelectric absorption screens; PHABS) from Balucinska-Church & McCammon (1992) was used to account for the Galactic absorption. The simplest isothermal gas model was considered for the fitting and expressed as PHABS × APEC using the Cash maximum-likelihood scheme (CSTAT) in XSPEC. Plasma abundances were fixed at 0.3 times the solar abundances, as this value is routinely found in the X-ray spectral fitting of young stars (e.g. Feigelson et al. 2002; Currie et al. 2009; Bhatt et al. 2013). The hydrogen column density ($N_{\rm H}$) and plasma temperature (kT) determined from the fitting were used to calculate the X-ray flux of the above 21 YSOs using the CFLUX model in XSPEC. For reference, we have shown a sample spectrum in Fig. 13. The X-ray fluxes of the remaining YSOs were derived from their X-ray count rates. The count conversion factor (CCF, i.e. 2.6×10^{-11} erg s^{-1} cm^{-2}) used to convert count rates into unabsorbed X-ray fluxes was estimated with WEBPIMMS[8] using the 1T APEC plasma model. The input parameters, kT ($\sim$2.7 keV) and $N_{\rm H}$ ($\sim 0.75 \times 10^{22}$ cm^{-2}), in WEBPIMMS were calculated as the mean of the kT derived from the spectral fitting of the 21 X-ray

---

[8] http://heasarc.gsfc.nasa.gov/cgi-bin/Tools/w3pimms/pim_adv

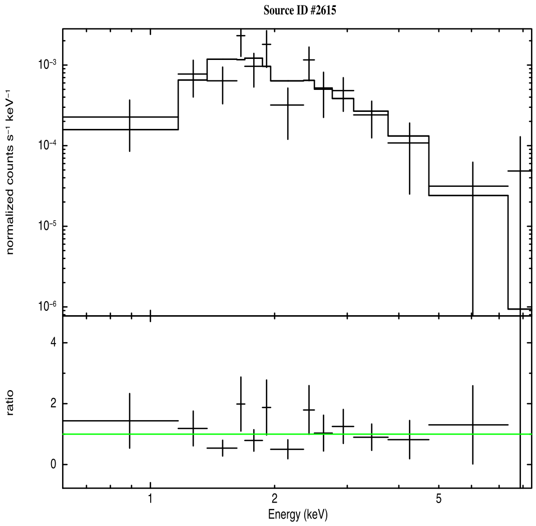

Figure 13. Example X-ray spectrum of a YSO (source ID 2615) fitted by the spectral model PHABS × APEC.

Table 7. Sample table containing the spectral parameters of the X-ray sources having NIR counterparts and identified as YSOs. IDs are the same as in Tables 3 and 4. The complete table is available in electronic form only.

ID	$N_{\rm H}$ (10^{22} cm^{-2})	kT (keV)	$\log(L_X(\mathrm{erg\,s^{-1}}))$
S_3	$0.45^{+0.18}_{-0.18}$	$0.59^{+0.33}_{-0.20}$	$31.67^{+0.07}_{-0.06}$
S_4	$0.68^{+0.17}_{-0.16}$	$0.65^{+0.18}_{-0.22}$	$31.85^{+0.06}_{-0.07}$
S_5	–	–	$30.59^{+0.34}_{-0.19}$
S_7	<0.39	$4.56^{+7.90}_{-2.16}$	$31.28^{+0.08}_{-0.08}$

sources that have counts greater than 35 and using the LAB model[9] (Kalberla et al. 2005), respectively.

Finally, the X-ray luminosities (L_X) for all 91 sources were estimated from the X-ray fluxes using the distance of NGC 7538, i.e. 2.65 kpc. The spectral parameters of these YSOs are given in Table 7. The $N_{\rm H}$ values for these X-ray sources are in the range 0.4–4.6 × 10^{22} cm^{-2}, which corresponds to an A_V range of 2–24 mag ($N_{\rm H} = 1.87 \times 10^{21} A_V$, Bohlin, Savage & Drake 1978), which is comparable to the A_V range of the YSOs in the present study (see Section 4.1). Therefore, we can safely assume that these sources are members of the NGC 7538 SFR.

4 DISCUSSION

4.1 Stellar parameters and X-ray properties of the candidate YSOs

In Section 3.2.1, we determined the stellar parameters of 463 YSOs using the SED fitting method. The YSOs that fall outside the distance range between 2.53 and 2.77 [i.e. $(D_s + \sigma_s) < (2.65–0.12)$ kpc or $(D_s - \sigma_s) > (2.65 + 0.12)$ kpc] as well as those that have a very low A_V [i.e. $A_{V_s} + \sigma_{A_{V_s}} < 2.8–0.2$ mag] were considered as non-members. In the above, D_s and σ_s are the distance and its error, and the corresponding values in kiloparsecs are 2.65 and 0.12. The foreground extinction magnitude and its error for the NGC 7538 region are 2.8 and 0.2 (see Appendix A). A total of 44 sources have been found to be in the foreground or background population and mistaken as associated YSOs and these are not used in further analyses. Therefore, we selected the remaining 419 YSOs as probable members of the NGC 7538 SFR (see Table 6).

Histograms of the age, mass and A_V of these YSOs are shown in Fig. 14. It is found that ∼91 per cent (380/419) of the sources have ages between 0.1 and 2.5 Myr. Similar results have been reported by Puga et al. (2010) and Balog et al. (2004). The masses of the YSOs are between 0.5 and 15.2 $M_\odot$, a majority (∼86 per cent) of them being between 0.5 and 3.5 $M_\odot$. These ages and masses are comparable with those of TTSs. Note that the derived masses of four YSOs are significantly higher than the cut-off limit of 8 $M_\odot$ for which one cannot separate observationally the luminosity due to accretion from the intrinsic luminosity of the protostar (Ward-Thompson & Whitworth 2011). The A_V distribution shows a long tail, indicating its large spread from A_V = 1–30 mag, which is consistent with the nebulous nature of this region. The average age, mass and extinction (A_V) for this sample of YSOs are 1.4 Myr, 2.3 $M_\odot$ and 11 mag, respectively.

The evolutionary class of the selected 419 YSOs given in Table 6 reveals that ∼24 per cent (99), ∼62 per cent (258) and ∼2 per cent (10) of the sources are class I, class II and class III YSOs, respectively. The remaining 52 could not be classified in the present study (see Section 3.1.2). The high percentage of class I/II YSOs indicates the youth of this region. We show in Fig. 15 (left-hand panel) the cumulative distribution of class I and class II YSOs as a function of their ages, which shows that class I sources are relatively younger than class II sources, as expected. We performed a Kolmogorov–Smirnov test for this age distribution, which indicates that the chance of the two populations having been drawn from the same distribution is ∼2 per cent. The right-hand panel of Fig. 15 plots the distribution of ages for the class I and class II sources. The distribution of the class I sources shows a peak at a very young age, i.e. $\lesssim$0.5 Myr, whereas that of the class II sources peaks at ∼1–1.5 Myr. Both of these figures were generated for the YSOs having masses greater than the completeness limit of this sample (i.e. >0.8 $M_\odot$) and they show an age difference of ∼1 Myr between the class I and class II sources. Note that Evans et al. (2009) through c2d *Spitzer* Legacy projects studied YSOs associated with five nearby molecular clouds and concluded that the lifetime of the class I phase is 0.54 Myr. The peak in the histogram of class I sources agrees well with this.

The stellar parameters of the X-ray emitting sources identified as YSOs can be used to study the possible physical origin of the X-ray emission in PMS stars. The coronal activity, which is primarily responsible for the generation of X-rays in low-mass stars, may be affected by the composition of the X-ray emitting plasma and the disc fraction during the PMS evolution in different classes of YSOs. A number of studies have been done for various SFRs, but no firm conclusion has been drawn so far on account of the contradictory results. In some cases, such as Chameleon I (Feigelson et al. 1993), ρ Ophiuchus (Casanova et al. 1995), IC 348 (Preibisch & Zinnecker 2002) and NGC 1893 (Pandey et al. 2014), no significant difference was found in the X-ray luminosity between class II and class III YSOs. However, there are several examples (Stelzer & Neuhäuser 2001; Flaccomio et al. 2003; Stassun et al. 2004; Preibisch et al. 2005; Flaccomio, Micela & Sciortino 2006; Telleschi et al. 2007b; Guarcello et al. 2012) that show that class II YSOs have lower X-ray luminosities than class III YSOs.

We derived L_X for 91 YSOs in the NGC 7538 region (see Section 3.3). A comparison of the X-ray activity of the YSOs in

---

[9] http://heasarc.gsfc.nasa.gov/cgi-bin/Tools/w3nh/w3nh.pl

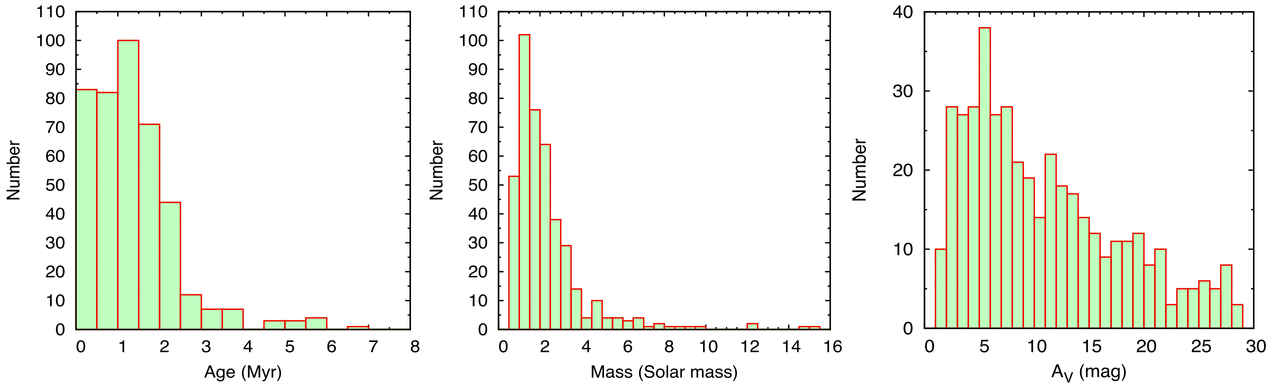

Figure 14. Histograms showing the distribution of the ages (left-hand panel), masses (centre panel) and extinction values A_V (right-hand panel) of the YSOs in the NGC 7538 region. The ages, masses and A_V are derived from the SED fitting analysis (see Section 3.2.1).

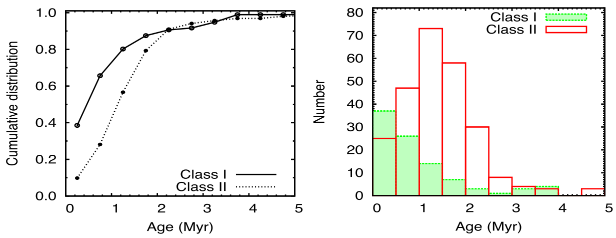

Figure 15. Left: Cumulative distribution of class I (solid line) and class II (dotted line) sources as a function of their age. Right: Age distribution of class I (filled histogram) and class II (unfilled histogram) sources.

Table 8. Results of two sample tests. Columns 2, 3 and 4 represent the probability that the samples have a common parent L_X distribution.

Test	Class I versus Class II	Class II versus Class III	Class I versus Class III
Wilcoxon rank sum	0.35	0.44	0.91
Peto and Peto generalized Wilcoxon	0.36	0.44	0.91
Kolmogorov–Smirnov	0.19	0.91	0.68
Anderson–Darling	0.16	0.44	0.43

different classes (class I: 20, class II: 34 and class III: 37) are shown in Fig. 16 with box plots and X-ray luminosity functions (XLFs) using the Kaplan–Meier estimator of integral distribution functions in the R package (version 3.2.0). The distribution shows that the X-ray activity is nearly similar in all YSO classes with a mean value of $\log{(L_X)}$ around 31.1 erg s^{-1}. The distribution of the class II YSOs shows a relatively larger scatter in comparison to those of the class I and class III sources. To derive the statistical significance of the comparison, we performed two sample tests for estimating the probability of having common parent distributions and the results are given in Table 8. They show that the X-ray activities in the class I, class II and class III objects are not significantly different from each other. It is thought that the X-ray activity in low-mass stars is associated mainly with the rotation rate and the depth of the convection zone. Our results may imply that the increase of the X-ray surface activity with an increase of the rotation rate is compensated for by the decrease of the stellar surface area during the PMS evolution (Preibisch 1997; Bhatt et al. 2013).

Out of the 91 YSOs with an L_X estimate (see Section 3.3), the age and mass have been estimated for 47 YSOs based on SED fitting. The masses of these YSOs is $>0.8\,M_\odot$. Note that the completeness limit for the X-ray emitting YSOs (64) is $0.8\,M_\odot$ (see Section 3.1.5).

To study the effect of circumstellar discs on the X-ray emission, in Fig. 17 we have tried to see if there is any correlation of L_X with age and mass. When drawing conclusions from these distributions,

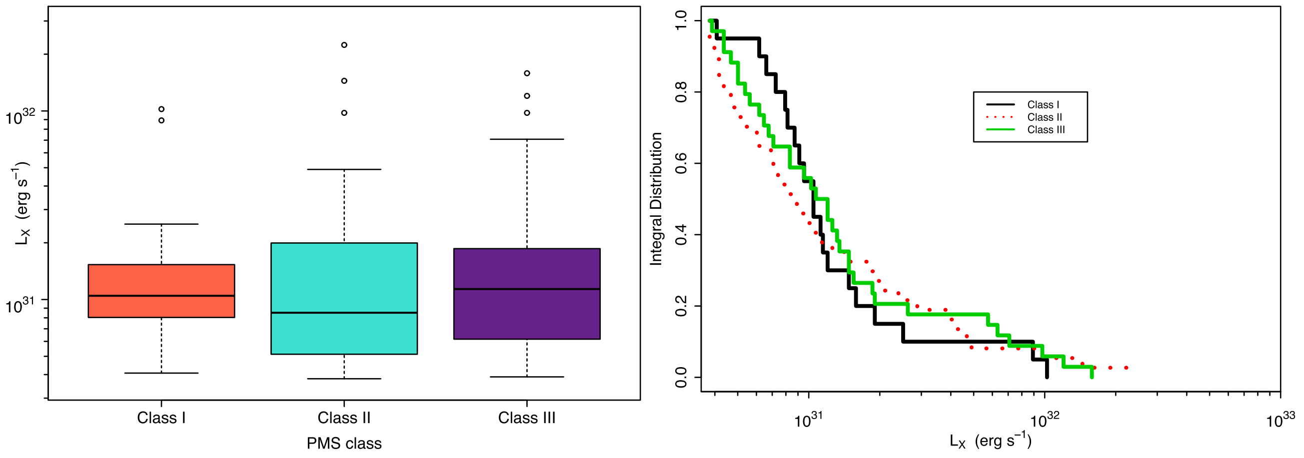

Figure 16. Left: Box plots of X-ray activity of class I, class II and class III objects. Data inferred from the upper and lower quartiles are shown with a box and its range. Open circles are the points outside 5 times the interquartile range above the upper quartile or below the lower quartile. Right: Comparison of the XLFs of class I, class II and class III objects.

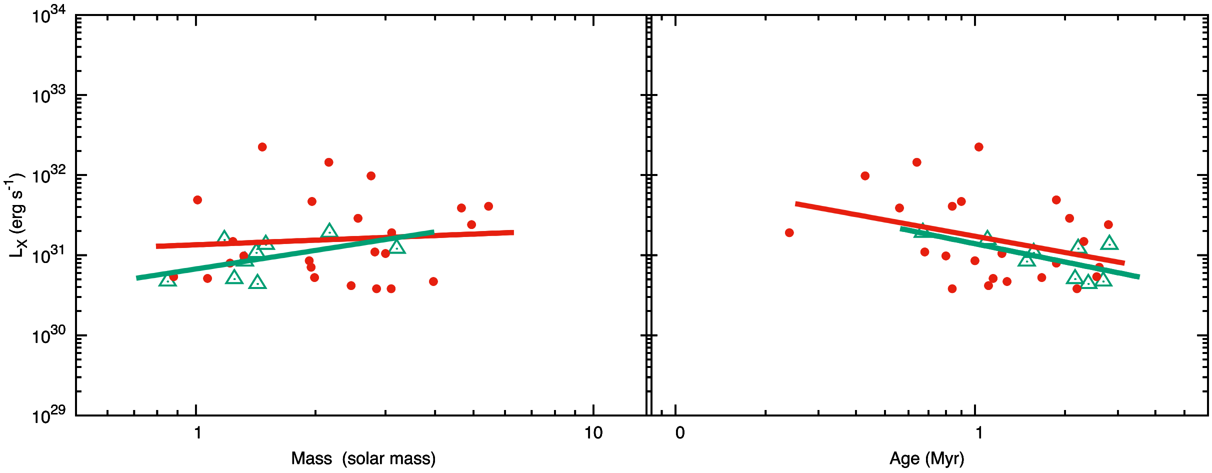

Figure 17. L_X versus mass and age in a logarithmic scale for the identified TTSs. Red dots and green triangles represent class II and class III YSOs, respectively. Red and green lines are the least-squares fit to the data for class II and class III sources, respectively.

Table 9. Coefficients of the straight lines fitted to the L_X versus mass/age distribution of the YSOs of different classes.

Class	Mass ($M_\odot$)	*a*	*b*	Age (Myr)	*a*	*b*
II	0.9–5.5	31.1 ± 0.2	0.2 ± 0.5	0.2–2.8	31.2 ± 0.1	-0.7 ± 0.4
III	0.9–3.2	30.8 ± 0.1	0.8 ± 0.5	0.7–2.8	31.1 ± 0.1	-0.8 ± 0.3

we have to be careful about the large errors in the estimated values of the ages and masses of the TTSs.

The L_X versus mass distribution shows a large scatter but with an indication of increasing L_X with mass for the class III sources. The values of coefficients *a* and *b* of the linear regression fit $\log(L_X) = a + b \times \log(M_\odot)$ for the class II and class III sources are given in Table 9. The intercepts *a* for the sources of different classes have comparable values to each other, indicating that the presence of circumstellar discs has practically no influence on the X-ray emission. This result agrees with that reported by Feigelson et al. (2002) and Pandey et al. (2014), and contradicts those by Stelzer & Neuhäuser (2001), Preibisch et al. (2005) and Telleschi et al. (2007a). There is an indication for a higher value of *b* for class III compared to class II sources. Recently, for a sample of class II and class III sources in the mass range 0.2–2.0 $M_\odot$ in the NGC 1893 region, Pandey et al. (2014) found the *b* values to be 0.51 ± 0.20 and 1.13 ± 0.13, respectively, whereas the *a* values were 30.71 ± 0.07 and 30.74 ± 0.05, respectively. Telleschi et al. (2007a) found $a = 30.13 \pm 0.09$ and 30.57 ± 0.09 and $b = 1.70 \pm 0.20$ and 1.78 ± 0.17 for class II and class III sources, respectively, in the Taurus molecular cloud. These slope values are higher than those obtained in the present study. One possible reason for the lower value for the NGC 7538 region may be a bias in our sample towards X-ray luminous, low-mass stars. For NGC 2264, the linear fit for the detected sources yields $a = 30.6 \pm 0.3$ and $b = 0.8 \pm 0.1$ (Dahm et al. 2007). However, after taking into account the X-ray non-detections, the slope is found to be steeper ($b = 1.5 \pm 0.1$). The mass range of YSOs used for the fitting also plays a crucial role, as already demonstrated by Guarcello et al. (2012). They found that for class III sources having mass ≤ 0.8 $M_\odot$ in NGC 6611, then slope $b = 1.1 \pm 0.3$, whereas the distribution of stars more massive than 0.8 $M_\odot$ is flatter with a slope of 0.4 ± 0.2.

L_X for both class II and class III sources can be seen to decrease systematically with age (in the age range ∼0.4 to 2.8 Myr). The values of the coefficients *a* and *b* of a linear regression fit $\log(L_X) = a + b \times \log(\mathrm{age})$ for the sources of different classes are given in Table 9. The nearly similar values of the intercept *a* and slope *b* for class II and class III indicates that circumstellar discs have practically no effect on the X-ray emission. Recently, Pandey et al. (2014) found $a = 35.06 \pm 0.63$ and 35.29 ± 0.65 and $b = -0.78 \pm 0.10$ and -0.81 ± 0.11, respectively, for their sample of class II and class III sources in NGC 1893. In NGC 7538, we found that the values of *a* for both class II and class III sources are much lower than those for NGC 1893, but the *b* values are almost like theirs. These are slightly steeper in comparison to those reported by Preibisch & Feigelson (2005, −0.2 to −0.5) and Telleschi et al. (2007a, -0.36 ± 011). This difference in the slope could be more significant for an unbiased sample where we expect more less luminous low-mass X-ray sources, which would give a higher value for the slope. If the X-ray luminosities for accreting PMS stars are systematically lower than for non-accreting PMS stars (e.g. Flaccomio et al. 2003; Preibisch et al. 2005) and if class II sources evolve to class III sources, one might expect that for a class II source, L_X should increase with age rather than decrease. However, the evolution of the class II sources up to ∼2.8 Myr does not show any sign of an increase in X-ray luminosity.

4.2 Triggered star formation

McCaughrean, Rayner & Zinnecker (1991) suggested there were YSOs at various evolutionary stages with considerable substructures in the vicinity of NGC 7538 (see Fig. 1). Here is a brief description of each of them.

IRS 1–3 This active region has three massive IR sources, each associated with its own compact H II region (Wynn-Williams et al. 1974). IRS 1 has been identified as a high-mass (∼30 $M_\odot$) protostar with a CO outflow, and is considered as the source that is injecting energy into the UC H II region NGC 7538 A (Puga et al. 2010). IRS 2, situated ∼10 arcsec north of IRS 1, is inferred to be an O9.5V star and possesses the most extended H II region. IRS 3 is situated about ∼15 arcsec west of IRS 1 (Ojha et al. 2004b) and is the least luminous of the three.

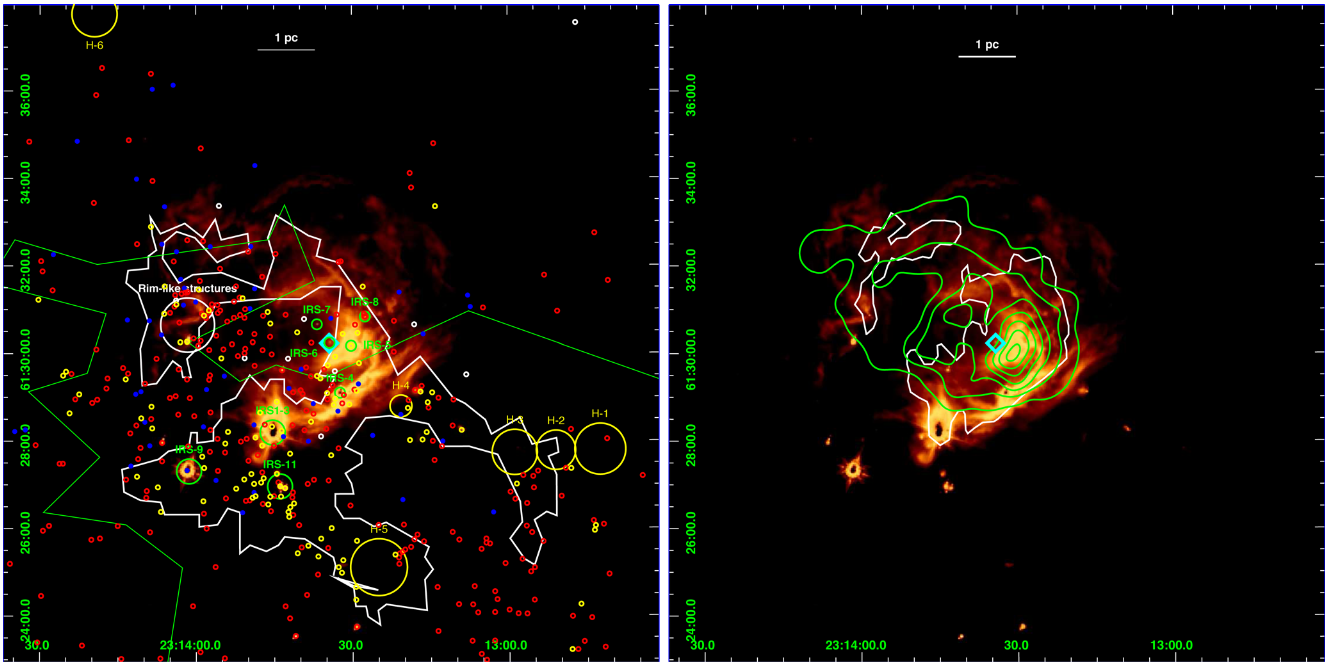

Figure 18. Left: Spatial distribution of the YSOs superimposed on the 15 × 15 arcmin IRAC 8.0 μm image of the NGC 7538 region. The location of class I (yellow circles), class II (red dots), class III (white dots) and unclassified (blue dots) sources are shown along with the $J = 1 - 0$ line of ^{13}CO (green contour) and 850 μm continuum emission (white contour) taken from Chavarría et al. (2014). Also shown are the positions of high-mass dense clumps (Fallscheer et al. 2013) along with the IR sources. Right: Distribution of the ionized gas as traced by radio (1280 MHz, green contours, Ojha et al. 2004b) and by Hα emission (white contours) shown overlaid on the IRAC 8.0 μm image of the same region.

IRS 4–8 This active region is a group of young stars located at the southern rim of the optical H II region IRS 4, a bright NIR reflection nebula containing an O9V star IRS 5, and the main ionizing source IRS 6 (O3V type) of the H II region NGC 7538 (Puga et al. 2010). IRS 7 and IRS 8 have been inferred as foreground field stars (Tsujimoto et al. 2005; Puga et al. 2010).

IRS 9 This bright reflection nebula located at the south-eastern tip of NGC 7538 harbours massive protostars (Werner et al. 1979; Pestalozzi et al. 2006; Puga et al. 2010).

IRS 11 This may be a large contracting or rotating filament that is fragmenting at scales of 0.1 to 0.01 pc to form multiple high-mass stars (∼10 $M_\odot$) having discs and envelopes as well as shedding outflows (Pestalozzi et al. 2006; Naranjo-Romero et al. 2012).

Rim-like structures (globules) This nebular region is on the north-eastern side of NGC 7538 and consists of two cone-shaped rim-like structures. Both point towards IRS 6 and have faint stars on their tip.

Apart from these active regions, Fallscheer et al. (2013) recently detected 13 more candidates for high-mass dense clumps in a 1 deg^2 field of NGC 7538. The positions and sizes of some of them are shown in Fig. 1 as H1 to H6, located mainly in the south-western periphery of NGC 7538. These are potential sites of intermediate- to high-mass star formation that could be identified through FIR observations by the *Herschel* space-based telescope.

Fig. 18 (left-hand panel) shows the spatial distribution of member YSOs (419 sources, see Section 4.1) superimposed on the IRAC 8.0 μm image of 15 × 15 arcmin^2 of the NGC 7538 region. This sample of YSOs is obtained from multiwavelength data taken from various surveys with different completeness limits. In Section 3.1.5, we discussed the completeness of these surveys and found that they can approximately be assumed complete for mass ≥0.8 $M_\odot$. A majority (94 per cent) of the YSOs selected here have masses ≥0.8 $M_\odot$, therefore, incompleteness in this sample will have a minimal effect on the overall spatial distribution of the YSOs.

The ^{13}CO $J = 1 - 0$ line (green contour) and 850 μm continuum (white contour) emission maps taken from Chavarría et al. (2014) are shown in Fig. 18 (left-hand panel). For simplicity, we have shown only the outermost contours, representing the extent of gas and dust in this region. The resolution of the ^{13}CO and 850 μm observations are 46 and 14 arcsec, respectively. Chavarría et al. (2014) found several groupings of YSOs in this region. They estimated the physical parameters of these groups and found that younger sources are in regions having YSOs with a higher surface density and are correlated with the densest molecular clouds. Since they did not discuss the effect of high-mass stars on recent star formation through the distribution of YSOs, gas and dust, we further used these distributions to trace star-formation activities in this region. The positions of the high-mass dense clumps (Fallscheer et al. 2013) along with the IR sources are also shown in the figure. In the right-hand panel of Fig. 18, the distributions of ionized gas as seen in the 1280 MHz radio continuum emission (green contours, Ojha et al. 2004b) and in Hα emission (white contours) are shown superposed on the IRAC 8.0 μm image of the same region. The YSOs are distributed either on the nebulosity or towards the southern regions.

The distribution of the ^{13}CO, 850 μm and Hα emission indicates a bubble-like feature around the ionizing source IRS 6, likely created due to the expansion of the H II region. The correlation of the PAH emission, as seen in the IRAC 8.0 μm image (Pomarès et al. 2009), with the ^{13}CO emission indicates that the ionized gas is confined inside the molecular cloud. The lack of diffuse emission at 8.0 μm can be noticed towards the south-east of IRS 6.

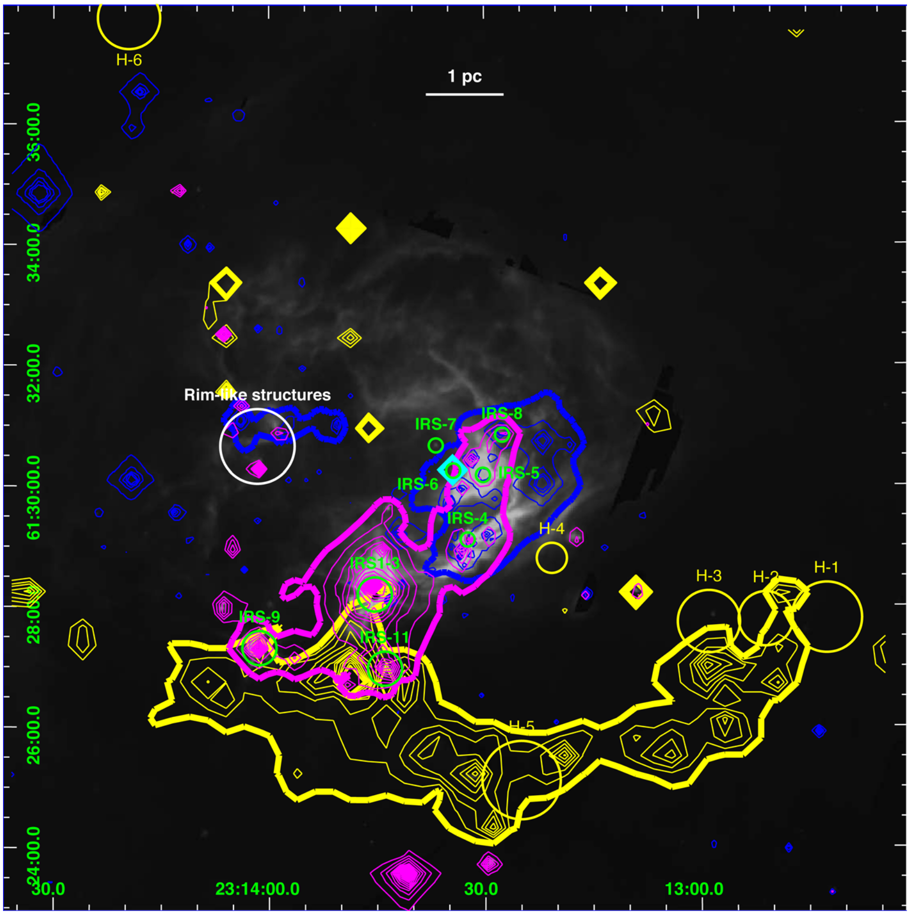

Figure 19. Distribution of younger (yellow contours), older (blue contours) and massive (purple contours) populations overlaid on the IRAC 8.0 μm image. The location of the IR sources, globules and cold clumps are also shown.

However, as can be seen from the radio continuum contours in Fig. 18 (right-hand panel), the ionized gas is bounded more sharply to the south-western region. The distribution of class I YSOs shows a nice correlation with that of molecular gas and the PAH emission/H II region boundaries. Very few class I sources are located towards the central region near IRS 6 compared to the outer southern regions. The strong positional coincidence between the YSOs and the molecular cloud suggests enhanced star-formation activity towards this region, as often observed in other SFRs (e.g. Evans et al. 2009; Fang et al. 2009). There is a concentration of very young YSOs (mainly class I) towards the southern region outside the dust rim (IRS 11). Five high-mass dense clump candidates (Fallscheer et al. 2013) are just outside the NGC 7538 H II region towards the south-west. There are many separate groups of younger YSOs near these cold molecular clumps. In summary, there are two main concentrations of YSOs, one in the H II region and the other in the southern region.

By analysing the distribution of YSOs of various ages and masses in relation to the molecular cloud structure, we can study the mode of star formation in this region. For this, we generated contour maps of the ages and masses of YSOs smoothed to the resolution of 9 arcsec grid size. In Fig. 19, we have over-plotted age contours on the IRAC 8.0 μm image representing younger (yellow contours) and comparatively older (blue contours) YSOs. The outermost age contours correspond to 0.7 and 1.8 Myr, respectively. In the same figure, we have also plotted the mass contours (purple) for the massive YSOs. The outermost contour corresponds to 4.2 M$_\odot$. The step sizes are 0.2 Myr and 0.2 M$_\odot$ for the age and mass contours, respectively. The older population is mainly associated with the H II region enclosed by thick blue contours, whereas the younger one is outside the H II region, mainly in the south-western part enclosed in a thick yellow contour. The mass distribution shows that the massive population, enclosed in the thick purple contours, is sandwiched between these two populations and is associated mainly with IRS 1–3, IRS 9 and IRS 11. The mean values of ages and masses of the YSOs associated with these subregions are given in Table 10.

Table 10. Mean values of ages and masses of YSOs in different regions.

Region	N	Mean mass (M$_\odot$)	Mean age (Myr)
Whole	419	2.3 ± 0.1	1.4 ± 0.1
South-west (young)	91	1.8 ± 0.1	1.0 ± 0.1
Central (old)	73	2.7 ± 0.2	2.0 ± 0.2
Central (old globules)	32	2.5 ± 0.2	1.9 ± 0.2
Central (old IRS 6)	41	2.9 ± 0.2	2.2 ± 0.2
South-central (massive)	35	4.7 ± 0.6	1.2 ± 0.2

The location of the IR sources, rim-like structures and the cold clumps are also shown in Fig. 19. The oldest region (thick blue contours) is made up of two separate groups, i.e. one around IRS 6

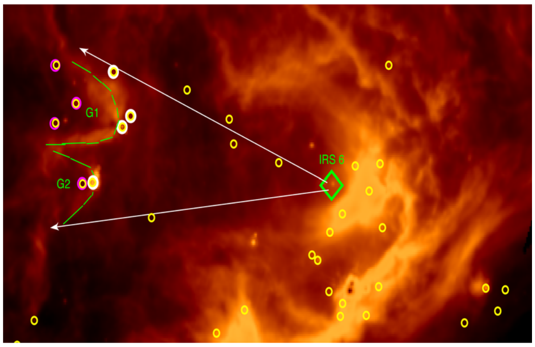

Figure 20. Location of the two globules along with the distribution of class I YSOs (circles) and IRS 6, the ionizing source of NGC 7538.

and the other near the rim-like structures (globules). The masses and ages of the YSOs near the rim-like structures are lower than those in the central region near IRS 6. The two rim-like structures with sharp edges (maybe due to the PAH emission) pointing towards the central star IRS 6 indicate that the ionization front interacts with the molecular ridge as seen in the ^{13}CO emission. They morphologically resemble bright-rimmed clouds that result from the pre-existing dense molecular clouds impacted by the ultraviolet photons from nearby OB stars (Lefloch & Lazareff 1994). The low-mass YSOs on their tips are generally believed to be formed as a result of the triggering effect of the expanding H II region (Deharveng et al. 2005; Zavagno et al. 2006; Koenig et al. 2008; Deharveng et al. 2009). Their elongated distribution and age difference with respect to the location of the ionization source can be used to check whether the RDI mode (Lefloch & Lazareff 1994; Miao et al. 2006) of triggered star formation was effective in the region.

For this purpose, we compared the time elapsed during the formation of the class I YSOs in the globule regions with the age and lifetime of the O3 ionization source. In Fig. 20, we show the location of the two globules, the ionizing source IRS 6 and the class I sources. The presence of extremely young class I sources presumably represents the very recent star-formation event in the region, thus can be taken as a proxy to trace the triggered star formation. The tips of the globules are at a projected distance of ∼2.4 pc from IRS 6. We estimated the time needed for the ionization front to travel there as ∼0.26 Myr, assuming that it expanded at a speed of ∼9 km s^{-1} (see e.g. Pismis & Moreno 1976). The age of the class I sources (white circles in Fig. 20) on this rim is 1.9 ± 0.6 Myr, which is ∼0.3 Myr younger than the estimated age of the O3V star (∼2.2 Myr, see Puga et al. 2010). The mean age of the class I sources inside the rim (magenta circles in Fig. 20) is 1.5 ± 0.6 Myr. We evaluated the shock crossing time in the globules to see whether the star formation there is initiated by the propagation of the shock or whether it had already taken place prior to the arrival of the shock. Assuming a typical shock propagation velocity of 1–2 km s^{-1}, as found for bright-rimmed clouds (see e.g. White et al. 1999; Thompson et al. 2004), the shock travel time to the YSOs, which are projected at distances ∼0.6 pc from the head, is ∼0.4 Myr. This time-scale is comparable to the difference in the ages of the YSOs on the rims and inside them. Although the sample is small and the errors are large, these results seems to support the notion that the formation of the YSOs in the globules could be due to the RDI mechanism. The above analysis is not statistically significant to conclude about the triggered star formation, but Dale et al. (2015) stated that a system where many indicators can be satisfied simultaneously may be a genuine site of triggering.

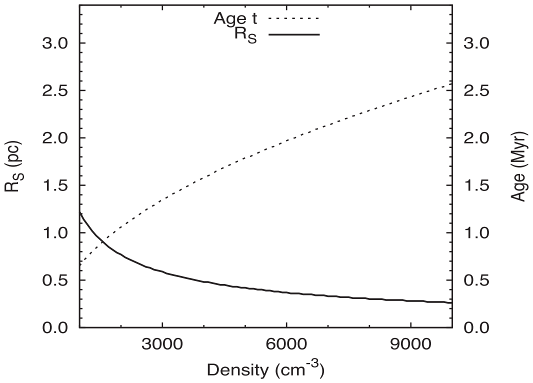

Figure 21. Plots showing the variation of the Strömgren radius and dynamical age with the ambient density.

Therefore, to investigate further, we calculated the dynamical age of the NGC 7538 H II region from its radius using the equation given by Spitzer (1978):

$$R(t) = R_{\rm S}\left(1 + \frac{7ct}{4R_s}\right)^{4/7},$$

where $R(t)$ denotes the radius of the H II region at time t, and c is the sound speed. The latter was assumed as ∼9 km s^{-1} (Pismis & Moreno 1976; Stahler & Palla 2005), and the former was taken to be 3 pc as derived from the radio and Hα maps (see Fig. 18). Then the dynamical age (t) can be calculated if we know the Strömgren radius $R_{\rm S}$, which is estimated using the relation given in Ward-Thompson & Whitworth (2011) and Stahler & Palla (2005) and by assuming an O3V star as the ionizing source emitting 7.4 × 10^{49} ultraviolet photons per second (Vacca, Garmany & Shull 1996). However, the initial ambient density is needed, which we do not know. So we have left it as a free parameter and calculated the Strömgren radius ($R_{\rm S}$) and the corresponding dynamical age (t) of the H II region for a range of ambient densities from 10^3 to 10^4 cm^{-3}. Fig. 21 shows the results, where $R_{\rm S}$ and t are plotted as functions of the initial ambient density. The former varies from ∼1.3 to 0.25 pc, while the latter varies from ∼0.7 to 2.6 Myr. This upper limit of the dynamical age is comparable to the age of the central O3 star and corresponds to a higher ambient density for this region. The mean age of the YSOs in this region is 1.4 Myr, which is less than the dynamical age of the region and, as such, their formation could have been influenced by the expanding H II region.

We also looked for the radial distance dependence of A_V, ages and masses of YSOs with respect to the ionizing source IRS 6 as shown in Fig. 22. As expected, the A_V distribution reveals less extinction near IRS 6 compared to the outer region. There is a broad peak starting at the projected distance of ∼3 pc and we see a decreasing trend after 5 pc. This seems to indicate the presence of a shell-like layer of collected medium just outside the H II region. It is very interesting to note that the age distribution shows a clear decrease from the centre to a distance of 3 pc. Also the masses of the YSOs within 3 pc are higher compared to those outside, indicating a difference in the physical properties of the YSOs within 3 pc. These trends are indicative of triggered star formation in the inner region (within 3 pc), where the O3 star played an active role. From 3 pc out, we see a completely different distribution with a large number of young and low-mass YSOs (see Table 10) in the south-west region of NGC 7538 (see Fig. 19, thick yellow contour). It seems that the YSOs in this group may have formed spontaneously in the absence of any triggering mechanism due to the O3 star. The distribution

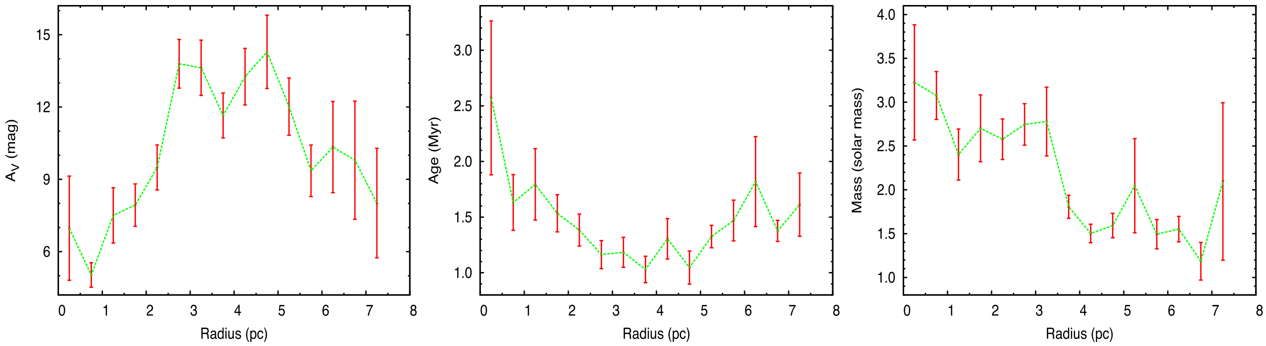

Figure 22. Distribution of A_V, age and mass of the YSOs as a function of radial distance from the ionizing source IRS 6.

of the cold clumps also suggests that spontaneous low-mass star formation is under way there. However, accurately disentangling triggered star formation from spontaneous star formation requires precise determination of the proper motions and ages of individual sources (Dale et al. 2015).

4.3 Mass function

The distribution of stellar masses that form in one star-formation event in a given volume of space is called the IMF. Together with the star-formation rate, it is one of the important issues in star-formation studies. Since the environmental effects due to the presence of high-mass stars may be more revealing at the low-mass end of the present-day MF, we will try to study it in the NGC 7538 SFR.

The MF is often expressed by a power law, $N(\log m) \propto m^{\Gamma}$ and the slope of the MF is given as $\Gamma = d \log N(\log m)/d \log m$ where $N(\log m)$ is the number of stars per unit logarithmic mass interval. The first empirical determination of MF was by Salpeter (1955), who gave $\Gamma = -1.35$ for the field stars in the Galaxy in the mass range $0.4 \le m/\mathrm{M}_{\odot} \le 10$. However, subsequent works (e.g. Miller & Scalo 1979; Scalo 1986; Rana 1991; Kroupa 2002) suggest that the MF in the Galaxy often deviates from a pure power law. It has been shown (see e.g. Scalo 1986, 1998; Kroupa 2002; Chabrier 2003, 2005) that, for masses above $\sim$1 $\mathrm{M}_{\odot}$, the MF can generally be approximated by a declining power law with a slope like that found by Salpeter (1955). However, it is now clear that this power law does not extend to masses below $\sim$1 $\mathrm{M}_{\odot}$. The distribution becomes flatter below 1 $\mathrm{M}_{\odot}$ and turns down at the lowest stellar masses. Kroupa (2002) divided the MF slopes for four different mass intervals. It was often claimed that some (very) massive SFRs have truncated MFs, i.e. contain much smaller numbers of low-mass stars than expected from the field MF. However, most of the recent and sensitive studies of massive SFRs (see e.g. Liu et al. 2009; Espinoza, Selman & Melnick 2009) have found large numbers of low-mass stars in agreement with the expectation from the normal field star MF. Preibisch et al. (2011) confirmed these results for the Carina Nebula and supported the assumption of a universal IMF (at least in our Galaxy). In consequence, this result also supports the notion that OB associations and massive star clusters are the dominant supply sources for the Galactic field star population, as already suggested by Miller & Scalo (1978).

As discussed earlier, the sample of YSOs used is compiled from various surveys with different completeness limits. So we tried to use only our deep and homogeneous optical data to generate the MF of the NGC 7538 region (see Sharma et al. 2007; Pandey et al. 2008, 2013; Chauhan et al. 2011; Jose et al. 2013). For this, we utilized the optical V versus $(V - I_c)$ CMD of all the sources in the NGC 7538 FOV and that of the nearby field region of equal area. We decontaminated the former sources of foreground and background stars using a statistical subtraction method. We show in Fig. 23 the $V/(V - I_c)$ CMDs for the stars lying within the NGC 7538 FOV (left-hand panel) and for those in the reference field region (middle panel). To subtract the latter from the former statistically, both CMDs were divided into grids of $\Delta V = 1$ mag by $\Delta(V - I_c) = 0.4$ mag. The number of stars in each grid of both CMDs was then counted and the probable number of cluster members in each grid was estimated from the difference. The estimated numbers of contaminating field stars (the numbers in the bin less the probable numbers of cluster members) were removed one by one from the cluster CMD that is the nearest to the randomly selected star in the CMD of the reference region of that bin.

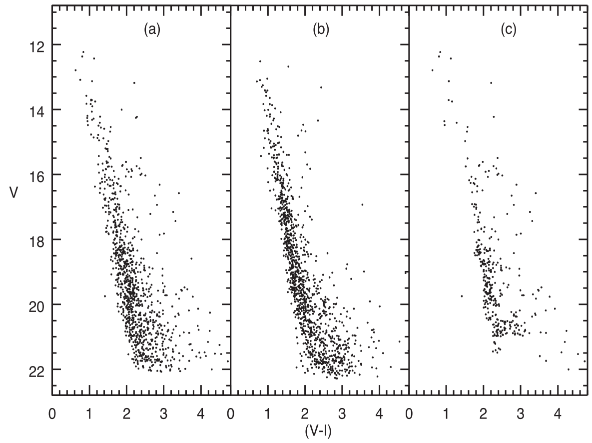

Figure 23. $V/(V - I_c)$ CMD for (a) stars in the NGC 7538 region and (b) stars in the reference region. (c) is a statistically cleaned CMD.

Both CMDs were also corrected for the incompleteness of the data. The photometric data may be incomplete due to various reasons, e.g. nebulosity, crowding of the stars, detection limit etc. In particular, it is very important to know the completeness limits in terms of mass. The IRAF routine ADDSTAR of DAOPHOT-II was used to determine the completeness factor (CF) (for details, see Sharma et al. 2008). Briefly, in this method artificial stars of known magnitudes and positions are randomly added into the original frames and then these artificially generated frames are re-reduced by the same procedure as used in the original reduction. The ratio of the number of stars recovered to those added in each magnitude gives the CF as a function of magnitude. To determine the completeness of the V versus $(V - I_c)$ CMD, we followed the procedure

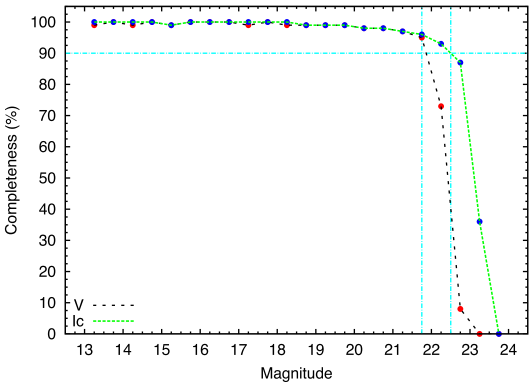

Figure 24. Completeness levels for the V and I_c bands (offset by 2 mag) as a function of magnitude derived from the artificial star experiments (ADDSTAR, see Section 4.3).

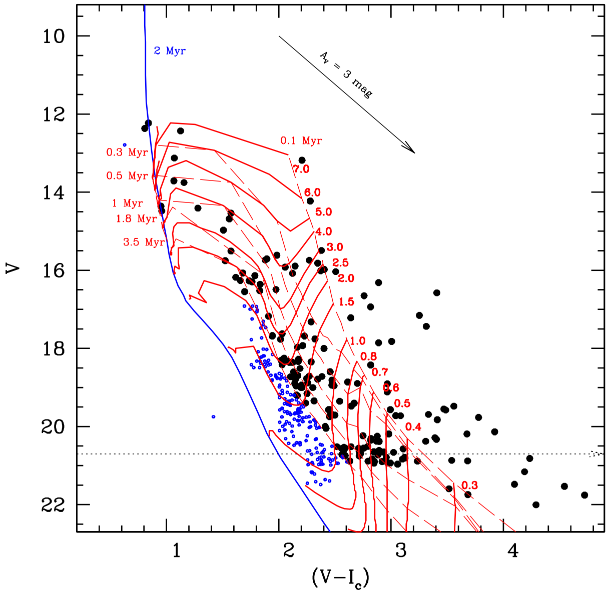

Figure 25. Statistically cleaned $V/(V - I_c)$ CMD for stars lying in the NGC 7538 region. Filled circles (ages $\lesssim$3.5 Myr) are used to estimate the MF of the region. The isochrone of 2 Myr from Marigo et al. (2008) and the PMS isochrones of 0.1, 0.3, 0.5, 1, 1.8 and 3.5 Myr along with the evolutionary tracks for different masses from Siess et al. (2000) are also shown. All the curves are corrected for the distance of 2.65 kpc and the foreground extinction $A_V = 2.1$ mag. The dashed horizontal line represents the completeness limit of the data after taking into account the average extinction of the YSOs.

given by Sagar & Richtler (1991), adding artificial stars to both V and I images in such a way that they have similar geometrical locations but differ in I brightness according to the mean $(V - I_c)$ colours of the MS stars. Since the mean $(V - I_c)$ colour of the MS stars is ~2 mag in the NGC 7538 region (see Fig. 23), the I-band magnitude is offset from the V-band magnitude by adding a correction of ~2 mag in Fig. 24, which shows the CF as a function of magnitude. As expected, the CF decreases with fainter magnitudes. Our photometry is more than 90 per cent complete up to $V \simeq 21.5$ mag, which corresponds to the detection limit of a 0.8 $M_\odot$ PMS star of age $\simeq$1.8 Myr (see Fig. 25) embedded in a nebulosity of $A_V \simeq 3.0$ mag (i.e. the average values for the optically detected YSOs, see Table 6).

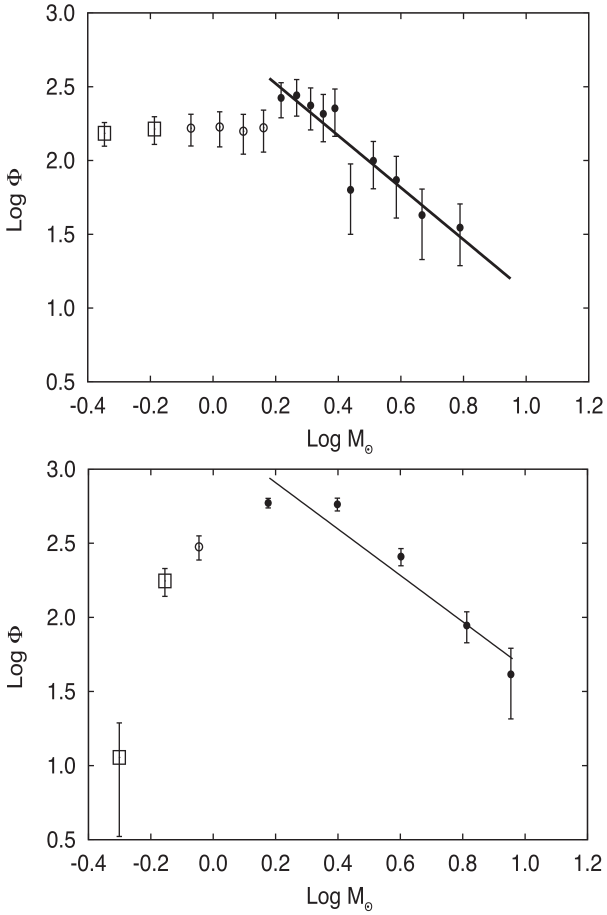

Figure 26. MF for the statistically cleaned CMD (top panel) and the identified YSOs (bottom panel) in the NGC 7538 region. $\log \phi$ represents $\log (N/d\log m)$. The error bars represent $\pm\sqrt{N}$ errors. The solid line shows a least-squares fit to the MF distribution (black dots). Open squares are the data points falling below the completeness limit of 0.8 $M_\odot$. Open circles are the data points near the turn-off point in the MF distribution and are not used in the fitting.

We have plotted in Fig. 25 the statistically cleaned $V/(V - I_c)$ CMD for the NGC 7538 region showing the PMS stars there. We have also plotted the zero-age-main-sequence (ZAMS) from Siess et al. (2000) and the PMS isochrones from Siess et al. (2000). The evolutionary tracks from Siess et al. (2000) for various masses have also been plotted. The dashed horizontal line represents the completeness limit of the data at $(V - I_c) = 2$ mag after taking into account the average extinction of the YSOs corrected for the distance.

The masses of individual stars were then estimated by the technique mentioned in Section 3.2.2, and the corresponding MF is plotted in Fig. 26 (upper panel). For this, we used only those sources that have ages equivalent to the average age of the optically identified YSOs combined with the error (i.e. $\lesssim$3.5 Myr, see Table 6). There is a change of slope from the high-mass to the low-mass end with a turn-off at around 1.5 $M_\odot$, as has often been noticed in other regions (Sharma et al. 2007; Pandey et al. 2008; Jose et al. 2008). The slope of the MF Γ for this sample in the mass range $\sim 1.5 < M/M_\odot < 6$ is -1.76 ± 0.24, which is steeper than the value -1.35 given by Salpeter (1955). We have optical photometry of only two IR sources associated with the NGC 7538 region, i.e. IRS 5 (O9, 20 $M_\odot$) and IRS 6 (O3, 60 $M_\odot$), as the others could not be resolved or are foreground sources. We did not use these two stars to generate the MF as they would have introduced large gaps between the points in the MF distribution and the corresponding errors would be quite large. Also, a lower mass range is required to compare this MF distribution to that of YSOs.

Since the detection limit for the optical sample is up to $A_V \simeq$ 7.7 mag (see Appendix A), the optical sample represents YSOs that are on the surface or partially embedded in the nebulosity of the NGC 7538 SFR. We need NIR and MIR data to cover the deeply embedded YSOs. In Section 3.2.1, with the help of the SED fitting, we estimated the age and mass of 419 YSOs using mostly NIR/MIR data. Therefore, we used this sample to trace deeper into the NGC 7538 region. The completeness limit for this sample, for which the data for individual YSOs are taken from various surveys, is discussed in Section 3.1.5 and found to be 0.8 $M_{\odot}$. The masses of the YSOs in this sample were used to generate the MF, which is shown in the lower panel of Fig. 26 (see also Kumar et al. 2014; Yadav et al. 2016). We have not used here the four high-mass YSOs (see Section 4.1). The slope of the MF Γ down to a similar mass limit (i.e. 1.5 $M_{\odot}$) for this sample of YSOs is -1.56 ± 0.27, which is like that, within the error, derived using optical CMD. From this, we can infer that the optical and SED fitting samples represent the same population of YSOs.

5 CONCLUSION

Although the NGC 7538 region has already been studied extensively in IR and radio wavelengths, it is rather neglected in the optical and X-ray. To the best of our knowledge, the present study is the first detailed multiwavelength study (including the optical) of this region. We have added some more YSOs based on their Hα or X-ray emission, thus complementing the previous IR excess based catalogue of the YSOs in the region. We have checked the association of these YSOs with NGC 7538 and derived their individual physical parameters based on the SED fitting. The spatial distribution of these YSOs along with those of the MIR and radio emission have been used to constrain the star-formation history in the region. The XLF and MF for the YSOs in this region have also been derived. The main results of this study can be summarized as follows:

(i) Analysis of the *Chandra* X-ray data in a ≈17 × 17 arcmin^2 field of the NGC 7538 region revealed 190 X-ray emitting sources.

(ii) Based on Hα grism spectroscopy, Hα (photometry) and X-ray emission, we have identified six, 15 and 64 YSOs, respectively, in the region. We have compiled a catalogue of 943 YSOs by combining those detected in the present study with those previously catalogued. 53 YSOs are new additions from this study. This new catalogue is complete down to 0.8 $M_{\odot}$.

(iii) We have derived the ages and masses of 463 YSOs based on the SED fitting analysis. 419 of them are confirmed to belong to the NGC 7538 SFR and ∼91 per cent (380/419) of them have ages between 0.1 and 2.5 Myr. A majority (∼86 per cent) of the 419 YSOs have masses between 0.5 and 3.5 $M_{\odot}$, as derived by the SED fitting analysis. These ages and masses are comparable with those of TTSs. The A_V value for these YSOs shows a spread from 1 to 30 mag. The average age, mass and extinction (A_V) for this sample of YSOs are 1.4 Myr, 2.3 $M_{\odot}$ and 11 mag, respectively.

(iv) Of the above 419 YSOs, around 24 per cent (99), 62 per cent (258) and 2 per cent (10) are found to be class I, class II and class III sources, respectively. The high percentage (∼85 per cent) of class I and class II YSOs indicates the youth of this region. A Kolmogorov–Smirnov test for the age distribution of the class I and class II sources suggests that it is different. The ages of class I sources are $\lesssim$0.5 Myr, whereas the class II sources have ages ∼1–1.5 Myr mostly, indicating an age difference of ∼1 Myr between them.

(v) The mean value of log (L_X) of YSOs identified in the region is found to be around 31.1 erg s^{-1}. It is found that the X-ray activities of the class I, class II and class III sources are not significantly different from each other. L_X seems to increase with the mass of the class III sources, whereas it decreases with the age of the class II and class III sources. However, we find no statistically significant difference in the slopes and intercepts for the L_X versus age distribution for the class II and class III sources, which indicates that the presence of circumstellar discs has practically no influence on the X-ray emission. This suggests that the increase of the X-ray surface activity with the increase of the rotation rate may be compensated for by the decrease of the stellar surface area during the PMS evolution.

(vi) The spatial distribution of the YSOs, along with the MIR, radio and CO emission, has been used to understand the star-formation process in the region. The YSOs in the inner region (within 3 pc from IRS 6 and containing the bright H II region) may have been formed by a triggering mechanism caused by the central high-mass star IRS 6.

(vii) The slope of the MF changes from the high-mass side to the low-mass side with a turn-off at around 1.5 $M_{\odot}$. The slope of the MF Γ in the mass range $1.5 < M/M_{\odot} < 6$ is -1.76 ± 0.24, which is steeper than the value in Salpeter (1955) of -1.35.

ACKNOWLEDGEMENTS

The authors are thankful to the anonymous referee for his/her useful comments. HB acknowledges the Inspire Faculty Grant Support (IFA11-PH02) of the Department of Science and Technology, India. The observations reported in this paper were obtained using the 1-m Sampurnanand Telescope, Nainital, India, and the 2-m HCT at IAO, Hanle, the High Altitude Station of the Indian Institute of Astrophysics, Bangalore, India. This publication makes use of data from the Two Micron All Sky Survey (2MASS), which is a joint project of the University of Massachusetts and the Infrared Processing and Analysis Center, California Institute of Technology, funded by the National Aeronautics and Space Administration and the National Science Foundation.

REFERENCES

Balog Z., Kenyon S. J., Lada E. A., Barsony M., Vinkó J., Gáspár A., 2004, AJ, 128, 2942
Balucinska-Church M., McCammon D., 1992, ApJ, 400, 699
Bertoldi F., 1989, ApJ, 346, 735
Bessell M. S., Brett J. M., 1988, PASP, 100, 1134
Bhatt H., Pandey J. C., Singh K. P., Sagar R., Kumar B., 2013, JA&A, 34, 393
Bica E., Dutra C. M., Barbuy B., 2003, A&A, 397, 177
Bohlin R. C., Savage B. D., Drake J. F., 1978, ApJ, 224, 132
Briceño C., Preibisch T., Sherry W. H., Mamajek E. A., Mathieu R. D., Walter F. M., Zinnecker H., 2007, in Reipurth B., Jewitt D., Keil K., eds, Protostars and Planets V. Univ. Arizona Press, Tucson, p. 345
Broos P. S., Townsley L. K., Feigelson E. D., Getman K. V., Bauer F. E., Garmire G. P., 2010, AJ, 714, 1582
Caramazza M. et al., 2012, A&A, 539, A74
Cardelli J. A., Clayton G. C., Mathis J. S., 1989, ApJ, 345, 245

Carpenter J. M., Snell R. L., Schloerb F. P., Skrutskie M. F., 1993, ApJ, 407, 657

Casanova S., Montmerle T., Feigelson E. D., Andre P., 1995, ApJ, 439, 752

Chabrier G., 2003, PASP, 115, 763

Chabrier G., 2005, in Corbelli E., Palla F., Zinnecker H., eds, Astrophysics and Space Science Library, Vol. 327, The Initial Mass Function 50 Years Later. Springer, Dordrecht, p. 41

Chauhan N., Pandey A. K., Ogura K., Ojha D. K., Bhatt B. C., Ghosh S. K., Rawat P. S., 2009, MNRAS, 396, 964

Chauhan N., Pandey A. K., Ogura K., Jose J., Ojha D. K., Samal M. R., Mito H., 2011, MNRAS, 415, 1202

Chavarría L., Allen L., Brunt C., Hora J. L., Muench A., Fazio G., 2014, MNRAS, 439, 3719

Chini R., Kruegel E., Kreysa E., 1990, A&A, 227, L5

Cohen J. G., Persson S. E., Elias J. H., Frogel J. A., 1981, ApJ, 249, 481

Crampton D., Georgelin Y. M., Georgelin Y. P., 1978, A&A, 66, 1

Currie T., Evans N. R., Spitzbart B. D., Irwin J., Wolk S. J., Hernandez J., Kenyon S. J., Pasachoff J. M., 2009, AJ, 137, 3210

Cutri R. M. et al., 2003, VizieR Online Data Catalog, 2246, 0

Dahm S. E., Simon T., Proszkow E. M., Patten B. M., 2007, AJ, 134, 999

Dale J. E., Haworth T. J., Bressert E., 2015, MNRAS, 450, 1199

Damiani F., Maggio A., Micela G., Sciortino S., 1997, ApJ, 483, 350

Deharveng L., Zavagno A., Caplan J., 2005, A&A, 433, 565

Deharveng L., Zavagno A., Schuller F., Caplan J., Pomarès M., De Breuck C., 2009, A&A, 496, 177

Deharveng L. et al., 2010, A&A, 523, A6

Dutta S., Mondal S., Jose J., Das R. K., Samal M. R., Ghosh S., 2015, MNRAS, 454, 3597

Elmegreen B. G., 1998, in Woodward C. E., Shull J. M., Thronson H. A., Jr, eds, ASP Conf. Ser. Vol. 148, Origins. Astron. Soc. Pac., San Francisco, p. 150

Elmegreen B. G., Lada C. J., 1977, ApJ, 214, 725

Espinoza P., Selman F. J., Melnick J., 2009, A&A, 501, 563

Eswaraiah C., Pandey A. K., Maheswar G., Chen W. P., Ojha D. K., Chandola H. C., 2012, MNRAS, 419, 2587

Evans N. J. II. et al., 2009, ApJS, 181, 321

Fallscheer C. et al., 2013, ApJ, 773, 102

Fang M., van Boekel R., Wang W., Carmona A., Sicilia-Aguilar A., Henning T., 2009, A&A, 504, 461

Favata F., Micela G., 2003, Space Sci. Rev., 108, 577

Feigelson E. D., Montmerle T., 1999, ARA&A, 37, 363

Feigelson E. D., Casanova S., Montmerle T., Guibert J., 1993, ApJ, 416, 623

Feigelson E. D., Broos P., Gaffney J. A., III, Garmire G., Hillenbrand L. A., Pravdo S. H., Townsley L., Tsuboi Y., 2002, ApJ, 574, 258

Flaccomio E., Damiani F., Micela G., Sciortino S., Harnden F. R., Jr, Murray S. S., Wolk S. J., 2003, ApJ, 582, 382

Flaccomio E., Micela G., Sciortino S., 2006, A&A, 455, 903

Frieswijk W. F., Spaans M., Shipman R. F., Teyssier D., Carey S. J., Tielens A. G. G. M., 2008, ApJ, 685, L51

Getman K. V. et al., 2005, ApJS, 160, 319

Golay M., 1974, Introduction to Astronomical Photometry, Astrophysics and Space Science Library Vol. 41. Reidel, Dordrecht, p. 375

Guarcello M. G., Caramazza M., Micela G., Sciortino S., Drake J. J., Prisinzano L., 2012, ApJ, 753, 117

Güdel M., 2004, A&AR, 12, 71

Guetter H. H., Vrba F. J., 1989, AJ, 98, 611

Gutermuth R. A., Megeath S. T., Pipher J. L., Williams J. P., Allen L. E., Myers P. C., Raines S. N., 2005, ApJ, 632, 397

Gutermuth R. A., Megeath S. T., Myers P. C., Allen L. E., Pipher J. L., Fazio G. G., 2009, ApJS, 184, 18

Haisch K. E., Jr, Lada E. A., Lada C. J., 2001, ApJ, 553, L153

Hartmann L., Megeath S. T., Allen L., Luhman K., Calvet N., D'Alessio P., Franco-Hernandez R., Fazio G., 2005, ApJ, 629, 881

He L., Whittet D. C. B., Kilkenny D., Spencer Jones J. H., 1995, ApJS, 101, 335

Herbig G. H., Bell K. R., 1988, Third Catalog of Emission-Line Stars of the Orion Population. Lick Observatory, Santa Cruz

Hernández J., Hartmann L., Calvet N., Jeffries R. D., Gutermuth R., Muzerolle J., Stauffer J., 2008, ApJ, 686, 1195

Hillenbrand L. A., Strom S. E., Vrba F. J., Keene J., 1992, ApJ, 397, 613

Hur H., Sung H., Bessell M. S., 2012, AJ, 143, 41

Jose J. et al., 2008, MNRAS, 384, 1675

Jose J. et al., 2013, MNRAS, 432, 3445

Jose J., Kim J. S., Herczeg G. J., Samal M. R., Bieging J. H., Meyer M. R., Sherry W. H., 2016, ApJ, 822, 49

Kalberla P. M. W., Burton W. B., Hartmann D., Arnal E. M., Bajaja E., Morras R., Pöppel W. G. L., 2005, A&A, 440, 775

Kendrew S. et al., 2012, ApJ, 755, 71

Koenig X. P., Allen L. E., Gutermuth R. A., Hora J. L., Brunt C. M., Muzerolle J., 2008, ApJ, 688, 1142

Koenig X. P., Leisawitz D. T., Benford D. J., Rebull L. M., Padgett D. L., Assef R. J., 2012, ApJ, 744, 130

Kroupa P., 2002, Science, 295, 82

Kumar B., Sharma S., Manfroid J., Gosset E., Rauw G., Nazé Y., Kesh Yadav R., 2014, A&A, 567, A109

Landolt A. U., 1992, AJ, 104, 340

Lee H.-T., Chen W. P., Zhang Z.-W., Hu J.-Y., 2005, ApJ, 624, 808

Lefloch B., Lazareff B., 1994, A&A, 289, 559

Lim B., Sung H. S., Karimov R., Ibrahimov M., 2011, J. Korean Astron. Soc., 44, 39

Liu Q., de Grijs R., Deng L. C., Hu Y., Baraffe I., Beaulieu S. F., 2009, MNRAS, 396, 1665

Luhman K. L., Allen P. R., Espaillat C., Hartmann L., Calvet N., 2010, ApJS, 186, 111

Mallick K. K., Ojha D. K., Samal M. R., Pandey A. K., Bhatt B. C., Ghosh S. K., Dewangan L. K., Tamura M., 2012, ApJ, 759, 48

Mallick K. K. et al., 2014, MNRAS, 443, 3218

Marigo P., Girardi L., Bressan A., Groenewegen M. A. T., Silva L., Granato G. L., 2008, A&A, 482, 883

Massi F., Giannetti A., Di Carlo E., Brand J., Beltrán M. T., Marconi G., 2015, A&A, 573, A95

McCaughrean M., Rayner J., Zinnecker H., 1991, Mem. Soc. Astron. Italiana, 62, 715

Meyer M. R., Calvet N., Hillenbrand L. A., 1997, AJ, 114, 288

Miao J., White G. J., Nelson R., Thompson M., Morgan L., 2006, MNRAS, 369, 143

Miller G. E., Scalo J. M., 1978, PASP, 90, 506

Miller G. E., Scalo J. M., 1979, ApJS, 41, 513

Moreno M. A., Chavarria K. C., 1986, A&A, 161, 130

Moscadelli L., Reid M. J., Menten K. M., Brunthaler A., Zheng X. W., Xu Y., 2009, ApJ, 693, 406

Naranjo-Romero R., Zapata L. A., Vázquez-Semadeni E., Takahashi S., Palau A., Schilke P., 2012, ApJ, 757, 58

Nisini B., Antoniucci S., Giannini T., Lorenzetti D., 2005, A&A, 429, 543

Ogura K., Sugitani K., Pickles A., 2002, AJ, 123, 2597

Ojha D. K. et al., 2004a, ApJ, 608, 797

Ojha D. K. et al., 2004b, ApJ, 616, 1042

Ojha D. K. et al., 2011, ApJ, 738, 156

Pandey A. K., Ogura K., Sekiguchi K., 2000, PASJ, 52, 847

Pandey A. K., Upadhyay K., Nakada Y., Ogura K., 2003, A&A, 397, 191

Pandey A. K., Sharma S., Ogura K., Ojha D. K., Chen W. P., Bhatt B. C., Ghosh S. K., 2008, MNRAS, 383, 1241

Pandey A. K. et al., 2013, ApJ, 764, 172

Pandey A. K., Samal M. R., Yadav R. K., Richichi A., Lata S., Pandey J. C., Ojha D. K., Chen W. P., 2014, New Astron., 29, 18

Panwar N., Chen W. P., Pandey A. K., Samal M. R., Ogura K., Ojha D. K., Jose J., Bhatt B. C., 2014, MNRAS, 443, 1614

Pestalozzi M. R., Minier V., Motte F., Conway J. E., 2006, A&A, 448, L57

Pestalozzi M. R., Elitzur M., Conway J. E., 2009, A&A, 501, 999

Phelps R. L., Janes K. A., 1994, ApJS, 90, 31

Pismis P., Moreno M. A., 1976, Revista Mexicana de Astronomía y Astrofísica, 1, 373

Pomarès M. et al., 2009, A&A, 494, 987

Preibisch T., 1997, A&A, 324, 690

Preibisch T., Feigelson E. D., 2005, ApJS, 160, 390

Preibisch T., Zinnecker H., 2002, AJ, 123, 1613
Preibisch T. et al., 2005, ApJS, 160, 401
Preibisch T. et al., 2011, A&A, 530, A34
Puga E. et al., 2010, A&A, 517, A2
Rana N. C., 1991, ARA&A, 29, 129
Rauw G., Manfroid J., De Becker M., 2010, A&A, 511, A25
Rivera-Ingraham A., Martin P. G., Polychroni D., Moore T. J. T., 2011, ApJ, 743, 39
Robitaille T. P., Whitney B. A., Indebetouw R., Wood K., Denzmore P., 2006, ApJS, 167, 256
Robitaille T. P., Whitney B. A., Indebetouw R., Wood K., 2007, ApJS, 169, 328
Robitaille T. P. et al., 2008, AJ, 136, 2413
Rowan-Robinson M., Gonzalez-Solares E., Vaccari M., Marchetti L., 2013, MNRAS, 428, 1958
Sagar R., Richtler T., 1991, A&A, 250, 324
Salpeter E. E., 1955, ApJ, 121, 161
Samal M. R., Pandey A. K., Ojha D. K., Chauhan N., Jose J., Pandey B., 2012, ApJ, 755, 20
Sandell G., Sievers A., 2004, ApJ, 600, 269
Sandell G., Wright M., 2010, ApJ, 715, 919
Sandell G., Goss W. M., Wright M., Corder S., 2009, ApJ, 699, L31
Sandford M. T., II, Whitaker R. W., Klein R. I., 1982, ApJ, 260, 183
Scalo J. M., 1986, Fundamental Cosmic Phys., 11, 1
Scalo J., 1998, in Gilmore G., Howell D., eds, ASP Conf. Ser. Vol. 142, The Stellar Initial Mass Function. Astron. Soc. Pac., San Francisco, p. 201
Schmidt-Kaler T., 1982, in Schaifers K., Voigt H. H., Landolt H., eds, Numerical Data and Functional Relationship in Science and Technology, Vol. 2b. Springer-Verlag, Berlin, p. 19
Sharma S., Pandey A. K., Ojha D. K., Chen W. P., Ghosh S. K., Bhatt B. C., Maheswar G., Sagar R., 2007, MNRAS, 380, 1141
Sharma S., Pandey A. K., Ogura K., Aoki T., Pandey K., Sandhu T. S., Sagar R., 2008, AJ, 135, 1934
Sharma S. et al., 2012, PASJ, 64, 107
Sharma S. et al., 2016, AJ, 151, 126
Siess L., Dufour E., Forestini M., 2000, A&A, 358, 593
Smith R. K., Brickhouse N. S., Liedahl D. A., Raymond J. C., 2001, ApJ, 556, L91
Spitzer L., 1978, Physical Processes in the Interstellar Medium. Wiley-Interscience, New York
Stahler S. W., Palla F., 2005, The Formation of Stars. Wiley-VCH, Weinheim
Stassun K. G., Ardila D. R., Barsony M., Basri G., Mathieu R. D., 2004, AJ, 127, 3537
Stelzer B., Neuhäuser R., 2001, A&A, 377, 538
Stetson P. B., 1987, PASP, 99, 191
Stetson P. B., 1992, in Worrall D. M., Biemesderfer C., Barnes J., eds, ASP Conf. Ser. Vol. 25, Astronomical Data Analysis Software and Systems I. Astron. Soc. Pac., San Francisco, p. 297
Sung H., Bessell M. S., Lee S.-W., 1997, AJ, 114, 2644
Telleschi A., Güdel M., Briggs K. R., Audard M., Palla F., 2007a, A&A, 468, 425
Telleschi A., Güdel M., Briggs K. R., Audard M., Scelsi L., 2007b, A&A, 468, 443
Thompson M. A., White G. J., Morgan L. K., Miao J., Fridlund C. V. M., Huldtgren-White M., 2004, A&A, 414, 1017
Thompson M. A., Urquhart J. S., Moore T. J. T., Morgan L. K., 2012, MNRAS, 421, 408
Tsujimoto M., Townsley L., Feigelson E. D., Broos P., Getman K. V., Garmire G., 2005, in Reipurth B., Jewitt D., Keil K., eds, Protostars and Planets V. Univ. Arizona Press, Tuscan, AZ, p. 8307
Vacca W. D., Garmany C. D., Shull J. M., 1996, ApJ, 460, 914
Wang J., Townsley L. K., Feigelson E. D., Getman K. V., Broos P. S., Garmire G. P., Tsujimoto M., 2007, ApJS, 168, 100
Ward-Thompson D., Whitworth A. P., 2011, An Introduction to Star Formation. Cambridge Univ. Press, Cambridge
Werner M. W., Becklin E. E., Gatley I., Matthews K., Neugebauer G., Wynn-Williams C. G., 1979, MNRAS, 188, 463
White G. J. et al., 1999, A&A, 342, 233
White R. J., Greene T. P., Doppmann G. W., Covey K. R., Hillenbrand L. A., 2007, in Reipurth B., Jewitt D., Keil K., eds, Protostars and Planets V. Univ. Arizona Press, Tuscan, AZ, p. 117
Whitney B. A., Wood K., Bjorkman J. E., Wolff M. J., 2003a, ApJ, 591, 1049
Whitney B. A., Wood K., Bjorkman J. E., Cohen M., 2003b, ApJ, 598, 1079
Whitney B. A., Indebetouw R., Bjorkman J. E., Wood K., 2004, ApJ, 617, 1177
Whittet D. C. B., 2003, Dust in the Galactic Environment, 2nd edn. IoP Publishing, Bristol
Whitworth A. P., Bhattal A. S., Chapman S. J., Disney M. J., Turner J. A., 1994, MNRAS, 268, 291
Williams J. P., Cieza L. A., 2011, ARA&A, 49, 67
Willis S., Marengo M., Allen L., Fazio G. G., Smith H. A., Carey S., 2013, ApJ, 778, 96
Wynn-Williams C. G., Becklin E. E., Neugebauer G., 1974, ApJ, 187, 473
Yadav R. K. et al., 2016, MNRAS, 461, 2502
Zavagno A., Deharveng L., Comerón F., Brand J., Massi F., Caplan J., Russeil D., 2006, A&A, 446, 171

SUPPORTING INFORMATION

Supplementary data are available at *MNRAS* online.

ONLINE-tables.tar.gz

APPENDIX A: DISTANCE AND REDDENING OF NGC 7538

NGC 7538 is in the second quadrant of the Galaxy in the Perseus arm. The distance estimates in the literature range from 2.2 kpc (Moreno & Chavarria 1986) to 2.8 kpc (Crampton, Georgelin & Georgelin 1978). The accuracy of these photometrically determined distances are typically 10–20 per cent. Puga et al. (2010) reported a spectro-photometric distance of 2.7 ± 0.5 kpc to this region. Moscadelli et al. (2009), using the trigonometric parallaxes of methanol masers, which are usually associated with high-mass SFRs, derived the most accurate distance of this region as $2.65^{+0.12}_{-0.11}$. Therefore, we have adopted 2.65 kpc as the distance for NGC 7538 in our analyses.

A $(U-B)/(B-V)$ TCD was used to estimate the amount of reddening towards the NGC 7538 region. In Fig. A1, we show the TCD with the intrinsic ZAMS (blue dotted curve) taken from Schmidt-Kaler (1982) along with the identified stars (black dots). For comparison, we have also over-plotted in Fig. A1 the 1 Myr isochrone (equivalent to ZAMS) from Marigo et al. (2008), which agrees well with that of Schmidt-Kaler (1982). The distribution of the stars shows a large spread along the reddening line, indicating heavy differential reddening in this region. It reveals two different populations, one (blue open circles) distributed along the ZAMS and another (black dots) showing a large spread in their reddening value. The former with negligible reddening must be the foreground population and the latter could be member stars. Both populations are selected visually based on their locations with respect to the ZAMS (for details, see Golay 1974; Phelps & Janes 1994). If we look at the MIR image of the NGC 7538 region (Fig. 1), we see several dust lanes along with enhancements of nebular emission at many places; both are likely responsible for the large spread of reddening in the latter population.

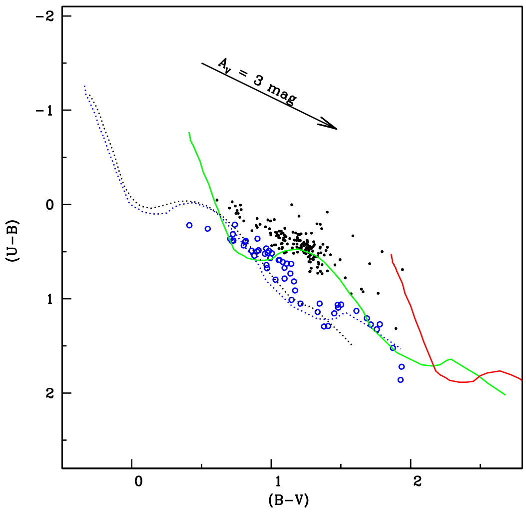

Figure A1. $(U-B)/(B-V)$ TCD for the sources in the NGC 7538 region. The dotted blue curve represents the intrinsic ZAMS for $Z = 0.02$ from Schmidt-Kaler (1982) along with the selected foreground stars (blue open circles). The 1 Myr isochrone (equivalent to ZAMS) from Marigo et al. (2008) is also shown as the black dotted curve. The continuous curves represent the Schmidt-Kaler (1982) ZAMS shifted along the reddening vector (see text for details) by $E(B-V)_{\mathrm{min}} = 0.75$ mag (green curve) and $E(B-V)_{\mathrm{max}} = 2.2$ mag (red curve) for reference to the stars embedded in the nebulosity of NGC 7538 (black dots).

The ZAMS from Schmidt-Kaler (1982) is shifted along the reddening vector with a slope of $E(U-B)/E(B-V) = 0.72 \times 0.91$ (corresponding to $R_V = 2.82$) to match the distribution of the stars showing the minimum reddening among the member population (green curve); this gives $E(B-V)_{\mathrm{min}} = 0.75$ and $A_V \simeq 0.75 \times 2.82 = 2.1$ mag. The others may be embedded in the nebulosity of the H II region. The ZAMS is further shifted along the reddening vector with a slope of $E(U-B)/E(B-V) = 0.72 \times 1.24$ (corresponding to $R_V = 3.85$) to match the distribution of these embedded stars showing the maximum reddening value, $E(B-V)_{\mathrm{max}} = 2.2$ mag [red curve, $A_V \simeq (0.75 \times 2.82 + 1.45 \times 3.85) = 7.7$ mag]. The approximate error in the reddening measurement of $E(B-V)$ is 0.2 mag, as determined by the procedure outlined in Phelps & Janes (1994).

APPENDIX B: REDDENING LAW

We used the technique described by Pandey et al. (2003) to study the nature of the diffuse interstellar medium (ISM) associated with the NGC 7538 region. This can be represented by the ratio of total-to-selective extinction $R_V = A_V/E(B-V)$. The normal reddening law for the solar neighbourhood gives the value $R_V = 3.1 \pm 0.2$ (Guetter & Vrba 1989; Whittet 2003; Lim et al. 2011), but for several SFRs, it is anomalously high (see e.g. Pandey, Ogura & Sekiguchi 2000; Pandey et al. 2008, 2013; Hur, Sung & Bessell 2012; Kumar et al. 2014).

The TCDs of the form of $(V-\lambda)$ versus $(B-V)$, where λ indicates one of the wavelengths of the broad-band filters (R, I, J, H, K, L), provide an effective method for separating the influence of the normal extinction produced by the general ISM from that of the abnormal extinction arising within regions having a peculiar distribution of dust sizes (see Chini, Kruegel & Kreysa 1990; Pandey et al. 2000). We selected all the stars having optical and NIR detections and plotted their $(V-\lambda)$ versus $(B-V)$ TCDs in Fig. B1. It reveals two distributions having different slopes. Presumably, the blue and black dots are the foreground population and the stars associated with NGC 7538, respectively, selected based on their reddening values (see Appendix A). Since YSOs (open circles) show excess IR emission, their position can deviate from those of the MS stars in the above TCDs, therefore they have not been used in the calculation of the reddening law. The slopes of the least-squares fit to the distribution of the MS member stars (black dots) in the $(V-I_c)$, $(V-J)$, $(V-H)$ and $(V-K)$ versus $(B-V)$ TCDs are found to be 1.44 ± 0.04, 2.47 ± 0.07, 2.95 ± 0.07 and 3.03 ± 0.06, respectively, which are higher than those found for the general ISM (1.10, 1.96, 2.42 and 2.60; see Pandey et al. 2003). On the other hand, the field population (blue dots) gives lower values for them (i.e. 1.12 ± 0.04, 1.75 ± 0.08, 2.26 ± 0.07 and 2.36 ± 0.06).

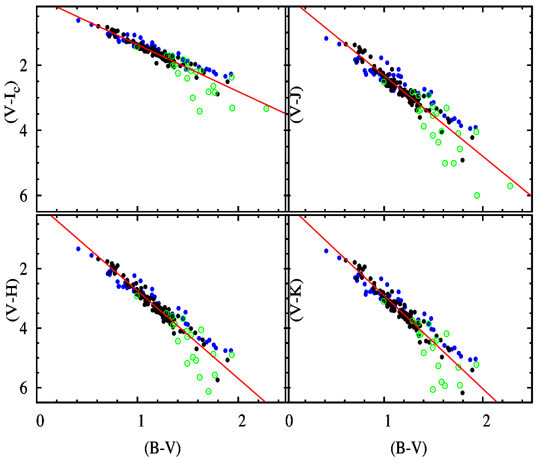

Figure B1. $(V-I_c)$, $(V-J)$, $(V-H)$ and $(V-K)$ versus $(B-V)$ TCDs for the stars associated with the NGC 7538 region (black dots) and for the foreground populations (blue dots) (see Appendix A). Open green circles are identified YSOs (see Section 3.1.4) and are not used in the analysis. Straight lines show the least-squares fit to the stars in the NGC 7538 region.

The slopes for the MS stars associated with the NGC 7538 region estimated as above yield a higher value for R_V (∼3.85 ± 0.15) (for a description of the reddening law estimation, see Pandey et al. 2003), indicating larger grain sizes of the material in this region compared to the general ISM. In many SFRs, R_V's tend to deviate from the normal value, preferably towards the higher ones, for example, $R_V = 3.7$ (Kumar et al. 2014, the Carina region), $R_V = 3.3$ (Pandey et al. 2013, NGC 1931), $R_V = 3.5$ (Sharma et al. 2012, NGC 281) and $R_V = 3.7$ (Pandey et al. 2008, Be 59). Within dense dark clouds, the accretion of ice mantles on grains and the coagulation due to grain collision can change the size distribution leading to higher R_V values (Cardelli et al. 1989). The value of R_V for the foreground population (blue dots in Fig. B1) towards the direction of NGC 7538 is ∼2.82 ± 0.10, indicating a slightly smaller grain size in the foreground medium of NGC 7538 compared to the general ISM. It is interesting that Eswaraiah et al. (2012) reported the mean value of R_V as 2.79 ± 0.18 for the general ISM towards the Be 59 SFR ($l = 118.22°$, $b = 5.00°$), which is in a similar direction to NGC 7538, based on polarimetric observations.

This paper has been typeset from a TEX/LATEX file prepared by the author.